The spatiotemporal dynamics of the sources and sinks of CO_2 in the global coastal ocean

Alizée Roobaert[1], Goulven G. Laruelle[1], Peter Landschützer[2], Nicolas Gruber[3], Lei Chou[1], and Pierre Regnier[1]

[1]Department of Geosciences, Environment & Society (DGES), Université Libre de Bruxelles, Brussels, CP160/02, Belgium.

[2]Max Planck Institute for Meteorology, Bundesstr 53, Hamburg, 20146, Germany.

[3]Environmental Physics, Institute of Biogeochemistry and Pollutant Dynamics, ETH Zürich, Universitätstrasse 16, 8092 Zürich, Switzerland.

Corresponding author: Alizée Roobaert (Alizee.Roobaert@ulb.ac.be)

Key Points:

- A new high-resolution monthly air-sea CO_2 flux climatology implies a global coastal ocean carbon sink of -0.20 ± 0.02 Pg C yr^{-1}.
- The zonal mean pattern of the air-sea CO_2 flux in coastal seas follows that of the adjacent open ocean except for river influenced regions.
- The seasonality of the coastal air-sea CO_2 exchange is largely driven by variations in seawater pCO_2 and temperature.

Abstract

In contrast to the open ocean, the sources and sinks for atmospheric carbon dioxide (CO_2) in the coastal seas are poorly constrained and understood. Here, we address this knowledge gap by analyzing the spatial and temporal variability of the coastal air-sea flux of CO_2 (FCO_2) using a recent high-resolution (0.25 degree) monthly climatology for coastal sea surface partial pressure in CO_2 (pCO_2). Coastal regions are characterized by CO_2 sinks at temperate and high latitudes and by CO_2 sources at low latitude and in the tropics, with annual mean CO_2 flux densities comparable in magnitude and pattern to those of the adjacent open ocean with the exception of river dominated systems. The seasonal variations in FCO_2 are large, often exceeding 2 mol C m^{-2} yr^{-1}, a magnitude similar to the variations exhibited across latitudes. The majority of these seasonal variations stems from the air-sea pCO_2 difference, although changes in wind speed and sea-ice cover can also be significant regionally. Globally integrated, the coastal seas act currently as a CO_2 sink of -0.20 ± 0.02 Pg C yr^{-1}, with a more intense uptake occurring in summer because of the disproportionate influence of high latitude shelves in the Northern Hemisphere. Combined with estimates of the carbon sinks in the open ocean and the Arctic, this gives for the global ocean, averaged over the 1998 to 2015 period an annual net CO_2 uptake of -1.7 ± 0.3 Pg C yr^{-1}.

1 Introduction

Globally, the ocean is currently taking up each year about 2.4 ± 0.5 Petagrams (Pg) of the extra (anthropogenic) carbon added to the atmosphere as a consequence of fossil fuel burning, cement production and land-use change (Le Quéré et al., 2018). While this global ocean uptake is well established on the basis of many independent methods (e.g., Gruber et al., 2009, 2019; Keeling & Manning, 2014; Landschützer et al., 2014; Manning & Keeling, 2006; Rödenbeck et al., 2015; Takahashi et al., 2012), the net carbon dioxide (CO_2) source/sink characteristic of the coastal ocean (a term equivalent to continental shelves in the present study) is still poorly known and subject to intense scientific debates. The discussion was launched two decades ago when Tsunogai et al. (1999) suggested, on the basis of an extrapolation of a single local study, that the coastal ocean takes up CO_2

from the atmosphere at a rate in excess of 1 Pg C yr^{-1} (note that by convention, a negative flux value corresponds to a CO_2 transfer from the atmosphere to the sea surface). Subsequent studies brought the coastal ocean uptake flux considerably down, with most estimates ranging from -0.45 Pg C yr^{-1} (Borges et al., 2005) to -0.21 Pg C yr^{-1} (Laruelle et al., 2010). The most important improvements consisted of a more adequate regional aggregation of the local/regional estimates before they were upscaled to the globe (Borges, 2005; Borges et al., 2005; Cai, 2011; Chen et al., 2013; Chen & Borges, 2009; Dai et al., 2013; Laruelle et al., 2010). But these estimates were still characterized by large uncertainties (Bauer et al., 2013; Regnier et al., 2013), primarily due to the limited number of observations (typically less than a hundred) available to derive local estimates of the coastal air-sea flux of CO_2 (FCO_2). A further important limitation was the relatively low granularity of the aggregation used in most upscaling studies, thus neglecting potentially important regional differences in the coastal air-sea CO_2 fluxes. Laruelle et al. (2014) overcame some of these limitations by using a fine aggregation level of 150 regional units, and computed globally an average coastal FCO_2 of -0.19 Pg C yr^{-1}. They improved the data coverage by taking advantage of the more than 3 million coastal measurements of the sea surface partial pressure of CO_2 (pCO_2) contained in the global database of the Surface Ocean CO_2 Atlas (SOCAT v2.0, Pfeil et al., 2013). Further, they used various upscaling methods depending on data coverage in the different regions. However, despite these improvements, the still rather poor sampling in many regions made such an aggregation-based upscaling method inherently uncertain, thereby limiting the constraints of these estimates, especially when considering the contribution of the coastal ocean to the global ocean carbon sink (Gruber, 2015). Further, the low spatial resolution of the Laruelle et al. (2014) estimates in many coastal regions did not allow them to evaluate consistently the spatial variability in the coastal environments, and the FCO_2 seasonal cycle could only be assessed for a restricted number of areas, mostly limited to the Atlantic basin.

Recently, Laruelle et al. (2017) generated a continuous high spatial resolution (0.25 degree) sea surface pCO_2 product for the coastal regions at monthly timescales for the period 1998-2015. They used a statistical interpolation method developed for the open ocean (Landschützer et al., 2013) and applied it for the first time in coastal regions. This method is based on neural network-inferred statistical

relationships between pCO_2 and a number of environmental variables (i.e., sea surface temperature, wind speed, bathymetry, …) that are known to control the pCO_2 variability in both time and space. This approach has the large advantage over the previously used aggregation methods in that it estimates relatively reliable pCO_2 values also in data poor regions, as long as other well sampled regions exist that have similar biogeochemical conditions permitting the neural network to be trained for such conditions (see also Rödenbeck et al., 2015). Relative to the work by Laruelle et al. (2014), the new product by Laruelle et al. (2017) also benefited from a substantial improvement of the data coverage in the SOCATv4 product (now 13.6 coastal million observations, Bakker et al., 2016; Sabine et al., 2013). This new high-resolution gridded monthly pCO_2 product for coastal regions provides the basis for a revised estimate of the global and regional coastal CO_2 sink/source characteristics at hitherto unprecedented resolution in time and space.

In addition to determining the global coastal carbon sink, we are particularly interested in the seasonal dynamics of the coastal air-sea CO_2 fluxes, as this provides insight into the sensitivity of these fluxes to environmental change. The few studies that attempted to identify and quantify the main processes driving the seasonality of FCO_2 remained, however, regional (Arruda et al., 2015; Frankignoulle & Borges, 2001; Nakaoka et al., 2006; Shadwick et al., 2010, 2011; Turi et al., 2014; Yasunaka et al., 2016) or were limited to a single oceanic basin (i.e., the Atlantic, Laruelle et al., 2014). In addition, with few exceptions (i.e. Yasunaka et al., 2016), most regional studies focused mainly on the seasonal variability of pCO_2, neglecting the potentially important contribution of changes in the atmospheric pCO_2, the gas transfer velocity and the sea-ice coverage. In the present study, we analyze for the first time the FCO_2 variability both in time and space in the global coastal ocean. We also quantify the major trends associated to the contribution of the sea-ice cover, the wind speed and the pCO_2 gradient variability.

2 Methodology

2.1 Air-sea gas exchange flux calculation

The air-sea gas exchange rate of CO_2 at the air-water interface (FCO_2, mol C m^{-2} yr^{-1}) is calculated using the diffusion-limited stagnant film model by Deacon (1977) given by:

$$FCO_2 = k\, K_0\, (1 - Ice)\, \Delta pCO_2 \quad (1)$$

A positive FCO_2 value corresponds to a transfer of CO_2 from the sea towards the atmosphere (i.e., source of CO_2 for the atmosphere) and a negative value corresponds to that from the atmosphere into the ocean (a sink of CO_2). K_0 represents the sea surface temperature (*SST*) and salinity (*SSS*) dependent solubility of CO_2 in water (mol C m^{-3} µatm^{-1}) and is calculated following Weiss (1974). ΔpCO_2 (µatm) is the difference in the partial pressure of CO_2 between the surface seawater ($pCO_{2,water}$, called hereafter pCO_2) and the atmosphere ($pCO_{2,air}$). *Ice* is a dimensionless coefficient corresponding to the fraction of the air-water interface (between 0 and 1) covered by sea-ice. k is the gas exchange transfer velocity of CO_2 (m yr^{-1}) calculated following Wanninkhof et al. (2009):

$$k = k_{660} \left(\frac{Sc}{660}\right)^{-1/2} \quad (2)$$

where k_{660} represents the gas exchange transfer velocity of CO_2 normalized to a temperature of 20 °C (for a *SSS* of 35) and is a function of the wind speed measured at 10 meters above the sea surface (U_{10}). Several coastal studies proposed k_{660}-relationships based on empirical methods for the CO_2 exchange in coastal seas (i.e., Jacobs et al., 1999; Kuss et al., 2004; Nightingale et al., 2000; Weiss et al., 2007) but these formulations were usually developed and calibrated locally or regionally (Roobaert et al., 2018). For our study, we use the quadratic formulation of Ho et al. (2011) with respect to wind speed ($k_{660} = cU_{10}^2$ where c is a constant value) which was calibrated with an extensive collection of k estimates in coastal environments. The Schmidt number (*Sc*, dimensionless) is calculated using the equation and parameterization given in Wanninkhof (2014):

$$Sc = A + B(SST) + C(SST)^2 + D(SST)^3 + E(SST)^4 \quad (3)$$

where A, B, C, D and E have constant values for CO_2 (for a *SSS* of 35) of 2116.8, -136.25, 4.7353, -0.092307, 0.0007555 respectively, and where *SST* is given in units of degrees Celsius.

2.2 Data

We compute the air-sea CO_2 flux (equation 1) for each 0.25 degree grid point in the coastal regions and for each month over the period 1998 to 2015 using the following data products: For pCO_2, we employ the monthly gridded product by Laruelle et al. (2017) at 0.25 degree resolution for coastal seas. This product was derived from 13.6 million coastal pCO_2 data contained in the Surface Ocean CO_2 Atlas version 4 (SOCATv4, Bakker et al., 2016; Sabine et al., 2013) and in LDEOv2015 (Takahashi et al., 2016) using a two-step artificial neural network interpolation technique (SOM-FFN), which allows one to produce contiguous high-resolution pCO_2 maps based on incomplete datasets. The SOM-FFN method generates pCO_2 values based on numerical relationships between independent environmental variables (i.e., *SST*, wind speed, bathymetry, …) and pCO_2 observations (see Landschützer et al., 2013, 2014, 2016 and Laruelle et al., 2017 for details regarding the method). The atmospheric partial pressures of CO_2 ($pCO_{2,air}$) are calculated from the dry air mixing ratio of CO_2 provided by the NOAA Marine Boundary Layer reference product assuming 100 % humidity (https://www.esrl.noaa.gov/gmd/ccgg/mbl/) and using the NCEP reanalysis total pressure at sea level (Kalnay et al., 1996). The monthly CO_2 solubility in seawater (K_0) is calculated following Weiss (1974) using monthly mean 0.25° *SST* and *SSS* derived respectively from the daily NOAA OI SST V2 (Reynolds et al., 2007) and the daily Hadley center EN4 SSS (Good et al., 2013) datasets. To calculate *k*, we use the monthly second moment of the 6 hour 0.25° global atmospheric reanalysis ERA-interim wind product (Dee et al., 2011) and the equation proposed by Wanninkhof (2014) for the Schmidt number (*Sc*) combined with the transformed *SST* field. The sea-ice cover is from the monthly mean of the daily 0.25° dataset of Reynolds et al. (2007) which is derived from Cavalieri et al. (1996) and Grumbine (1996). We use the most recent versions of these data sets, which cover our entire analysis period (1998-2015). Note that their referencing corresponds to the original release of these databases. From the full time series, we then compute a monthly climatology of the coastal FCO_2 and of all other relevant parameters (*SST*, etc).

2.3 Spatial analysis and comparison with the open ocean

Following Laruelle et al. (2013, 2014), the outer limit of the coastal region corresponds approximately to the shelf break. Estuaries and inland water bodies are not considered in this study and the total surface area of the coastal domain is 28 million km^2. FCO_2 and spatially integrated FCO_2 (Tg C yr^{-1}) are also analyzed regionally using a division of the continental shelves into 45 regions. This delineation is based on the Margins and CATchment Segmentation (MARCATS, Laruelle et al., 2013) which describes coastal regions characterized by similar climatic and hydrological settings. These 45 MARCATS, represented in Figure 1, can also be grouped into 7 major classes based on hydrology and climate following the classification proposed by Liu et al. (2010): (1) Eastern and (2) Western Boundary Currents (EBC and WBC respectively), (3) tropical margins, (4) subpolar and (5) polar margins, (6) marginal seas and (7) Indian margins. For each MARCATS, our results are compared to those calculated in previous studies based on observational data (Laruelle et al., 2014) and on results from an Oceanic General Circulation/Biogeochemical Model (Bourgeois et al., 2016). These two studies use the same definition of the coastal region and take into account the effect of the sea-ice cover in their FCO_2 calculations.

The air-sea CO_2 exchange dynamics in the coastal region is also compared to the climatological air-sea CO_2 fluxes of the open ocean for the 1998-2015 period. Monthly FCO_2 values are calculated for the open ocean following the same protocol as for the coastal seas (see section 2.1) except for the spatial resolution, which is limited to 1° x 1°, identical to that of the oceanic pCO_2 climatology of Landschützer et al. (2017) (see Landschützer et al., 2016 for the method) and for the calculation of the k value. The datasets used for monthly sea-ice cover, wind speed, *SST*, *SSS* and $pCO_{2,air}$ are the same as those used for the coastal calculations. These latter ones are aggregated into the 1° x 1° cells of the open ocean product by performing surface weighted averages of the 16 0.25° cells comprised within each 1° x 1° cell. We use a quadratic k_{660}-formulation developed for a global scale FCO_2 calculation based on the ^{14}C inventory method (Sweeney et al., 2007; Takahashi et al., 2009; Wanninkhof, 1992, 2014) to

calculate k. Because the ^{14}C inventory method is applied to the entirety of the global ocean, it is suitable to derive k for the open ocean but not for the coastal seas where other regional process than wind driven turbulence may disturb the gas exchange at the air-water interface. In order to limit uncertainties on k associated to the wind product at its specific spatio-temporal resolution (Roobaert et al., 2018), we rescale the coefficient c to fit to a global average gas exchange transfer velocity of 16 cm h^{-1} (Wanninkhof et al., 2013) for the period of our study. The open ocean domain is delineated by a land-sea mask from Landschützer et al. (2017) excluding the Arctic Ocean basin and coastal regions. Cells overlapping both oceanic and coastal domains are removed from the open ocean. The resulting open ocean covers a total surface area of 311 x 10^6 km^2.

2.4 Seasonality analysis

To explore the drivers of the seasonal FCO_2 variability in the coastal regions, we follow the strategy developed by Doney et al. (2009) and Couldrey et al. (2016) and construct, for each climatological month, spatial maps of the FCO_2 anomaly (FCO_2'). For each grid cell, the monthly FCO_2 anomaly is calculated as the difference between the FCO_2 for a given month and the climatological annual mean $\overline{FCO_2}$:

$$FCO_2' = FCO_2 - \overline{FCO_2} \quad (4)$$

where FCO_2' and FCO_2 represent the anomaly and the air-sea CO_2 exchange rate calculated for each month, respectively.

A positive FCO_2' for a given month implies that the FCO_2 is a stronger source or a weaker sink of CO_2 for the atmosphere during that month compared to the 1998-2015 mean FCO_2 while a negative value implies a stronger sink/weaker source. In our seasonal analysis, winter consists of the months of January, February and March in the Northern Hemisphere and of July, August and September in the Southern hemisphere. We then decompose the drivers of the seasonal FCO_2 variability following the procedure described by Couldrey et al. (2016) to isolate the contributions of the different factors to the total FCO_2 variability. Using a Reynolds decomposition for turbulent flow, the monthly variability of a term z which is a function of 3 forcing components ($z = wxy$) can be expressed as:

$$z' = (wxy)' \tag{5}$$

$$z' = (w'\bar{x}\bar{y}) + (\bar{w}x'\bar{y}) + (\bar{w}\bar{x}y') + \left[\left(w'x'y' - \overline{w'x'y'}\right) + \left(w'x'\bar{y} - \overline{w'x'\bar{y}}\right) + \left(w'\bar{x}y' - \overline{w'\bar{x}y'}\right) + (\bar{w}x'y' - \overline{\bar{w}x'y'})\right] \tag{6}$$

In this study we apply this decomposition to equation 1. z and z' thus represent FCO_2 and its anomaly calculated for each month, respectively. The terms w and x correspond to the sea-ice cover and ΔpCO_2 drivers, respectively. The term y corresponds to the combined effects of k and K_0, which isolates the wind speed driver since the product of $cU_{10}^2\left(\frac{Sc}{660}\right)^{-\frac{1}{2}}K_0$ is invariant with temperature (Etcheto & Merlivat, 1988; Wanninkhof, 2014). Equation 6 can then be expressed as:

$$FCO_2' = \left((1-ice)'\overline{\Delta pCO_2}(\overline{kK_0})\right) + \left(\overline{(1-ice)}\Delta pCO_2'(\overline{kK_0})\right) + \left(\overline{(1-ice)}\overline{\Delta pCO_2}(kK_0)'\right) + \left[\left((1-ice)'\Delta pCO_2'(kK_0)' - \overline{(1-ice)'\Delta pCO_2'(kK_0)'}\right) + \left((1-ice)'\Delta pCO_2'\overline{(kK_0)} - \overline{(1-ice)'\Delta pCO_2'\overline{(kK_0)}}\right) + \left((1-ice)'\overline{\Delta pCO_2}(kK_0)' - \overline{(1-ice)'\overline{\Delta pCO_2}(kK_0)'}\right) + \left(\overline{(1-ice)}\Delta pCO_2'(kK_0)' - \overline{\overline{(1-ice)}\Delta pCO_2'(kK_0)'}\right)\right] \tag{7}$$

The first three terms on the right hand side of equation 7 represent the seasonal FCO_2 anomaly from a long-term annual mean induced by the variability of the sea-ice cover ($(1-ice)'\overline{\Delta pCO_2}(\overline{kK_0})$, term 1), of the air-sea pCO_2 gradient ($\overline{(1-ice)}\Delta pCO_2'(\overline{kK_0})$, term 2) and of the wind speed ($\overline{(1-ice)}\overline{\Delta pCO_2}(kK_0)'$, term 3), respectively. Terms comprised between the large brackets correspond to the cross-correlation between the three drivers and are treated as a single term (term 4, sum of the four terms) in this study. The sum of all terms on the right-hand side of equation 7 is identical to the seasonal FCO_2 anomaly calculated in equation 4.

In order to evaluate how much a driver contributes to the monthly FCO_2', we calculate, for each grid cell, the slope (β) of a simple linear regression between monthly FCO_2' and monthly values resulting from the different drivers (terms 1 to 4 in equation 7). For example, for the contribution to the FCO_2' induced by the seasonal variability of the wind speed, β is calculated as follows:

$$\frac{\partial FCO_2'}{\partial(1-ice)\Delta pCO_2(kK_0)'} = \beta_{wind} \tag{8}$$

A value of β equal to 1 means that the term analyzed explains entirely the FCO_2 anomaly while a value of 0 means that FCO_2' is insensitive to that term. When β is greater than 1, the particular term produces larger anomalies than FCO_2', which are compensated by anomalies of opposite sign and are attributed to other terms. The sum of all the β terms adds up to 1, when including the cross-correlation terms.

2.5 Uncertainty analysis

For both the open ocean and coastal regions, the FCO_2 uncertainty stems from the combination of the uncertainties associated with the different terms of equation 1 used to calculate FCO_2 : (1) the air-sea pCO_2 gradient constrained by the water pCO_2 field generated by the SOM-FFN interpolation method (σ_{pCO2}, Landschützer et al., 2014, 2018; Laruelle et al., 2017), (2) the choice of the k_{660}-formulation for the gas exchange transfer velocity (σ_k) and (3) the choice of the wind product (σ_{wind}, Roobaert et al., 2018). Considering that these three sources of error are independent from each other and following the strategy used in Landschützer et al. (2014, 2018), we calculate the total error (σ) as the square root of the sum of the three squared errors:

$$\sigma = \sqrt{\sigma_{pCO2}^2 + \sigma_k^2 + \sigma_{wind}^2} \tag{9}$$

We estimate the flux uncertainty associated to the wind product (σ_{wind}) as the standard deviation of the CO_2 flux obtained using three different wind products, namely the ERA-interim (Dee et al., 2011), the Cross-Calibrated Multi-Platform Ocean Wind Vector 3.0 (Atlas et al., 2011) and the NCEP/NCAR reanalysis 1 (Kalnay et al., 1996). We exclude the widely used NCEP/DOE AMIP-II Reanalysis (Kanamitsu et al., 2002) climatology from our analysis because of its lesser constrained values at the air-water interface (Roobaert et al., 2018; Winterfeldt & Weisse, 2008). Calculations are performed for each wind product following the method described in sections 2.1 and 2.2 to produce three sets of FCO_2. For the open ocean, the fluxes are calculated by adjusting the value of c for each wind product

(see Roobaert et al., 2018, for further details). σ_k is estimated, for both the open ocean and the coastal regions, as the FCO_2 standard deviation resulting from the use of four k_{660}-formulations applied to the same wind field (ERA-interim). We apply the formulations of Ho et al. (2011), Sweeney et al. (2007), Takahashi et al. (2009) and Wanninkhof (2014), all of which are suitable for global-scale applications. There exist numerous formulations of k in coastal environments which but those are designed from and for regional studies (Roobaert et al., 2018). We thus decided to follow the same strategy and equations (other than the one from Ho et al., 2011) for our uncertainty analysis in the coastal ocean as the strategy applied to the open ocean for the sake of consistency. The uncertainty of the pCO_2 gradient across the air water interface (σ_{pCO2}) is the result of the uncertainty in both the oceanic and atmospheric pCO_2. However, the uncertainty of atmospheric pCO_2 is much lower than that of the oceanic pCO_2 (Landschützer et al., 2018) permitting us to assume that the uncertainty associated to the pCO_2 gardient at the air-water interface can be entirely attributed to that of oceanic pCO_2 (θ_{pCO2}). The latter can be decomposed into 3 sources of uncertainty: θ_{map} (the uncertainty obtained by comparing the pCO_2 products derived from the SOM-FFN with gridded observations from the SOCAT database), θ_{grid} (the uncertainty resulting from the gridding of the original SOCAT observations into a 1° open ocean grid and a 0.25° coastal grid) and θ_{obs} (the experimental uncertainty associated to pCO_2 measurements in the field). For a given region (i.e., MARCATS or oceanic basin), each source of uncertainty is divided by the square root of its degree of freedom, which is equal to the number of pCO_2 samples (N) collected in the region, except for θ_{map}, for which N is corrected using the lag 1 autocorrelation coefficient to evaluate the effective sample size (N_{eff}), following a procedure described in Landschützer et al. (2018). The calculation of the lag 1 autocorrelation coefficient involves the random selection of 1000 data points within each region. In order to generate the most robust uncertainties possible, the procedure is repeated 10 times and the final value of N_{eff} is the median generated by these 10 ensemble runs.

$$\theta_{pCO2} = \sqrt{\left(\frac{\theta_{obs}}{\sqrt{N}}\right)^2 + \left(\frac{\theta_{grid}}{\sqrt{N}}\right)^2 + \left(\frac{\theta_{map}}{\sqrt{N_{eff}}}\right)^2} \quad (10)$$

In our calculations, θ_{map} is calculated as the root mean squared deviation between the pCO_2 field and the gridded observations from SOCAT over the region of interest. θ_{grid} is considered to be 5 µatm following the estimate of Sabine et al. (2013) for the open ocean. We assume the same value for the coastal ocean in spite of the different spatial resolutions (i.e., 1 degree and 0.25 degree for the open and coastal oceans, respectively). θ_{obs} is considered to be 2 µatm following Pfeil et al. (2013). Finally, the uncertainty on the FCO_2, σ_{pCO2} (in mol C m^{-2} yr^{-1}) resulting from the uncertainty on the pCO_2 field (θ_{pCO2}, in µatm), is obtained by applying equation 1 to the global θ_{pCO2} field. Globally, the averaged biaises between pCO_2 generated by the SOM-FFN algorithm and observations are null for the open ocean and coastal seas (Landschützer et al., 2014; Laruelle et al., 2017). At the scale of MARCATS, however, a few regions with significant biaises have been identified in coastal seas (i.e., the Peruvian upwelling, MARCATS 4, the Moroccan upwelling, MARCATS 22, as well as along the western Arabian Sea, MARCATS 27; Laruelle et al., 2017). However, considering their relatively small cumulated surface area compared to the global coastal ocean (~ 1 %), the influence of theses biaises on the global coastal FCO_2 is negligible and no biais correction was performed.

3 Results

3.1 Spatial distribution

In the climatological annual mean (Figure 2a), about two-thirds of the coastal 0.25° x 0.25° grid points act as sinks for atmospheric CO_2, while the remaining one-third are sources or are near-neutral. The CO_2 sink regions are mainly found at temperate and high latitudes (i.e., poleward of 30°) and the strongest sources occur in the tropics. Globally, the dominance of sinks over sources leads to a sizeable average uptake FCO_2 density of -0.58 mol C m^{-2} yr^{-1}, which amounts to a global uptake of -195 Tg C yr^{-1} (-0.20 Pg C yr^{-1}) over the 1998 through 2015 period. Our global mean flux density is very close to

the -0.51 mol C m^{-2} yr^{-1} estimate of Laruelle et al. (2014) once their original value (-0.7 mol C m^{-2} yr^{-1}) is adjusted for the presence of sea-ice.

The global pattern of the coastal air-sea CO_2 fluxes becomes clearer when the fluxes are integrated by MARCATS regions (Figure 3a and Table S1). As already indicated by the grid point level analysis above, the vast majority of the MARCATS (31 over 45, 71 % of the total surface area of the coastal seas) act as a sink for atmospheric CO_2. The strongest and most consistent sink regions are found in the polar and subpolar coastal seas. The South Greenland region (MARCATS 15) has the highest sink strength, taking up annually -2.90 mol C m^{-2} yr^{-1}, closely followed by the Norwegian basin (MARCATS 16). On average, the marginal seas also act as sinks, but the spread among them is very large with three regions presently acting as sources, i.e., the Gulf of Mexico (MARCATS 9), the Red Sea (MARCATS 28) and the Persian Gulf (MARCATS 29). On the other hand, the Black Sea (MARCATS 21) has the second largest uptake flux density of MARCATS regions. All Western Boundary Current (WBC) regions are sinks, but with a relatively modest average flux density. The Eastern Boundary Current (EBC) regions are also moderate sinks, but with a somewhat larger spread as well as one region emitting CO_2 to the atmosphere (Moroccan upwelling, MARCATS 22). In this region, the SOM-FFN technique underestimates the observed pCO_2 because of the scarcity in data to train the algorithm (Laruelle et al., 2017). The resulting FCO_2 yields thus only a weak source of CO_2 for the atmosphere while observations suggest a more intense evasion (Laruelle et al., 2014). The remaining 31 % of the MARCATS that release CO_2 into the atmosphere are all located in the tropical coastal regions and in the Indian Ocean, except for the West Arabian Sea, MARCATS 27. The strongest source is observed in the Persian Gulf (MARCATS 29) with a FCO_2 value of 0.85 mol C m^{-2} yr^{-1}. The 31 MARCATS sink regions absorb altogether -219 Tg C yr^{-1} while the 14 MARCATS source regions release only 25 Tg C yr^{-1}. The most important contribution to the global sink (Figure 3b) is provided by the polar/subpolar margins (-143 Tg C yr^{-1} over 14 MARCATS), followed by the marginal seas (-43 Tg C yr^{-1} over 9 MARCATS). The WBCs and the EBCs also act as CO_2 sink with integrated FCO_2 values of -19 Tg C yr^{-1} (5 MARCATS) and -9 Tg C yr^{-1} (6 MARCATS), respectively. The tropical margins (15 Tg C yr^{-1}, 7 MARCATS) and the Indian margins (4 Tg C yr^{-1}, 4 MARCATS) act as sources.

3.2 Comparison with the open ocean

The spatial distribution of the mean FCO_2 for the 1998 through 2015 period from the Landschützer et al. (2017) pCO_2 product for the open ocean is overall remarkably similar to that found along the continents (Figures 2a and 2b). As discussed by Landschützer et al. (2014), the strong outgassing in the tropical regions are overcompensated by the strong uptake in the temperate regions and the high latitude North Atlantic (see also Takahashi et al., 2009; Gruber et al., 2009). Globally, the open ocean acts as a net sink of CO_2 for the atmosphere with a global mean FCO_2 of -0.37 mol C m^{-2} yr^{-1}. This value is 36 % lower than that calculated here for the coastal regions (-0.58 mol C m^{-2} yr^{-1}).

There are a few regions, however, where the coastal flux densities diverge quite substantially from those in the adjacent open ocean (Figures 2a and 2b). Most of these differences correspond to regions influenced by large rivers which include, in the Atlantic basin, the mouths of the two large Argentinean estuaries (the Rio de la Plata and the Bahia Blanca) which act as sources in opposition to negative FCO_2 values recorded in the surrounding adjacent open ocean. In contrast the Amazon plume acts as a sink (< -1 mol C m^{-2} yr^{-1}) while the adjacent open ocean is a source. In the Indian basin, differences are observed near the mouths of Zambezi and Pungwe rivers (southeast of Africa) and along part of the coast of Madagascar. Conversely, in Southeast Asia, coastal seas are generally FCO_2 sources while the surrounding open ocean takes up CO_2. In the Pacific basin, negative FCO_2 values are observed along the coast and near the Baja California Peninsula coast while FCO_2 is positive in the adjacent open ocean. Two other regions, namely in the western Arabian Sea and in the Peruvian upwelling current (MARCATS 27 and 4, respectively), also present contrasted differences with the open ocean. But these differences need be considered with caution due to limitations of the neural network technique of Laruelle et al. (2017) in regions where only limited data are available for calibration, and for which no other region with similar biogeochemical conditions can be found for training. These two regions are characterized by strong upwelling that are known to create very high and variable pCO_2 values (see e.g., Friederich et al. (2008) for the Peruvian upwelling). Yet, the neural network estimates of Laruelle et al. (2017) suggest very low pCO_2 values, creating sinks in the coastal regions, whereas the adjacent open

ocean in both the western Arabian Sea and eastern tropical Pacific are strong sources. We thus regard the coastal flux estimates in these two upwelling regions as questionable.

To emphasize the similarity of the air-sea CO_2 fluxes in the open ocean and in the coastal regions, we analyze the zonal mean profiles in Figure 4a. For both open and coastal ocean, Northern latitudes (> 40° N) are characterized by intense sinks(< -1 mol C m^{-2} yr^{-1}) followed by an increase of FCO_2 towards values close to equilibrium with the atmosphere. With the exception of the latitudinal bands comprised between 60°- 45° in both hemispheres where the coastal regions are more intense CO_2 sinks than the open ocean, FCO_2 is higher in the open ocean than in the coastal regions at most latitudes. In the tropics, the coastal and the open ocean are both sources of CO_2 for the atmosphere. However, the latitudinal band where the open ocean releases CO_2 (15° N - 15° S) is more restricted compared to that of the coastal ocean which expands from 30° N to 20° S. Around the equator, however, coastal seas exhibit FCO_2 values close to the equilibrium while the open ocean displays its strongest source (1.29 mol C m^{-2} yr^{-1}) mainly driven by the equatorial Pacific upwelling. At more austral latitudes, both the coastal and the open ocean act as CO_2 sinks, with a progressive increase in FCO_2 until 40° S. South of 60° S, FCO_2 values are close to equilibrium with the exception of a pronounced source around 60° S.

Although the meridional distribution of the average flux density FCO_2 is relatively similar between the open and coastal ocean, the integrated FCO_2 shows very different patterns (Figure 4b and c). This results primarily from the large differences in the surface areas. Due to the wide distribution of the coastal regions north of 60° N (7.1 million km^2 which represents 25 % of the total surface area of the coastal seas) and to the presence of intense FCO_2 sinks there, more than one-third of the global coastal ocean uptake is provided by these regions, taking up -98 Tg C yr^{-1} (Table 1). In contrast, only a small fraction (6 %, -87 Tg C yr^{-1}) is provided by the open ocean regions > 60° N, almost entirely due to the small surface area of the open ocean in those regions (1 %). Another sink is located in the coastal seas along the Pacific basin where -54 Tg C yr^{-1} is taken up (when the seas of Japan and Okhotsk are included) followed by the Atlantic basin (-27 Tg C yr^{-1}, Gulf of Mexico included). Marginal seas (-18 Tg C yr^{-1}), and the coastal in the Southern Ocean (south of 45° S, -17 Tg C yr^{-1}) and in the Indian Ocean where the latter represents a source of CO_2 (10 Tg C yr^{-1}), contribute to less than 10 % to the global

uptake. By combining the open ocean and coastal fluxes estimated using the two pCO_2 climatologies of Landschützer et al. (2017) and Laruelle et al. (2017) respectively, we can now assess, for the first time, the true global ocean uptake flux of CO_2 (Table 1). To this end, we also need to account for the uptake flux in the Arctic ocean basin which is not included in the pCO_2 climatology of Landschützer et al. (2017). Using an estimate of -0.12 ± 0.06 Pg C yr^{-1} for the Arctic basin by Schuster et al. (2013) which excludes the Baffin Bay and Nordic seas, the global net uptake of CO_2 by the entire ocean for the 1998 to 2015 period amounts to -1.7 ± 0.3 Pg C yr^{-1}. At the basin scale, the combined continental coastal/open ocean estimate reveals that all oceans act as a CO_2 sink for the atmosphere with a relatively equal contribution between the Atlantic (-393 Tg C yr^{-1}, 25 % of the global uptake), the Pacific (-386 Tg C yr^{-1}, 25 %) and the Indian (-322 Tg C yr^{-1}, 20 %) followed by the Southern Ocean (-275 Tg C yr^{-1}, 18 %).

3.3 Seasonality analysis

The global spatial distribution of the amplitude of the seasonal cycle in the air-sea CO_2 exchange flux for coastal regions is presented in Figure 5a, expressed as the root-mean-square (RMS) for each grid cell of the monthly FCO_2 anomalies (FCO_2'). Globally, the average $\mathrm{RMS}_{FCO_2'}$ of the seasonal cycle of all grid cells taking into account their variable surface area is 0.8 mol C m^{-2} yr^{-1}. In general, high seasonal variabilities (i.e., high $\mathrm{RMS}_{FCO_2'}$) are found in the Northern Hemisphere from mid- to high-latitudes and in the Southern hemisphere south of 40° S. In contrast, the equatorial and tropical regions exhibit less pronounced seasonal variability except for some local areas such as the Amazon estuarine plume. The seasonal amplitude in grid cells located at high latitudes (> 40° in both hemispheres) can reach values (i.e., 2 mol C m^{-2} yr^{-1}) comparable to the difference in the mean FCO_2 density observed between the polar and equatorial regions (Figure 3). The spatially averaged $\mathrm{RMS}_{FCO_2'}$ aggregated at the larger spatial scale of the MARCATS regions (Figure 6) reveals that only three MARCATS have a seasonal variability with a $\mathrm{RMS}_{FCO_2'}$ exceeding 1 mol C m^{-2} yr^{-1}. They are all localized in marginal seas (Baltic Sea, MARCATS 18, Black Sea, MARCATS 21 and the Hudson Bay, MARCATS 12) with the highest

seasonal variability observed in the Baltic Sea ($RMS_{FCO_2'}$ of 3.4 mol C m^{-2} yr^{-1}). Among the other regions, $RMS_{FCO_2'}$ values > 0.5 mol C m^{-2} yr^{-1} are mostly found in polar and subpolar coastal seas, in most of the marginal seas as well as in one or two MARCATS of the EBC (the Iberian upwelling, MARCATS 19) and the WBC (the Florida upwelling, MARCATS 10, and the Yellow sea, MARCATS 39).

The temporal distribution of the FCO_2' seasonal cycles for different latitudinal bands is shown in Figure 5b to 5f. These bands were selected in order to (1) compare the seasonal dynamics between the two hemispheres consistently and (2) evaluate the seasonal dynamics between high, mid- and low latitudes. For each latitudinal band, monthly FCO_2' are calculated from the mean of the surface weighted average FCO_2' of all grid cells pertaining to that band. Their seasonal amplitude is also presented in each panel ($RMS_{FCO_2'}$). The latter is calculated from the mean seasonal profile and consequently can be lower than the average of all grid cells for a given latitudinal band.

The seasonal cycle is more pronounced at higher latitudes and in regions with a strong seasonal signal (> 40° in both hemispheres), $RMS_{FCO_2'}$ values vary from 0.5 to 0.7 mol C m^{-2} yr^{-1}. The amplitude of the seasonal variability at lower latitudes between 40° S and 40° N is smaller with a $RMS_{FCO_2'}$ value of 0.25 mol C m^{-2} yr^{-1}. At low latitudes between 10° N and 10° S, the amplitude of the seasonal cycle is very low compared to other latitudinal bands (not shown in Figure 5, see Figure 8 for further details). Overall, FCO_2 seasonal cycles are very similar within the same latitudinal bands in both hemispheres. Generally, the largest difference in FCO_2 intensity between seasons is observed between summer and winter except for the temperate region between 40° - 60° in both hemispheres where they are observed in spring and fall. At high latitudes (> 60° in both hemispheres), FCO_2' reaches its minimum (most negative FCO_2' value indicating the strongest sink/weakest source) in summer and its maximum (most positive FCO_2' value indicating the strongest source/weakest sink) in winter. These two extremes are slightly shifted in time between 40° - 60° in both hemispheres where they are observed during spring and fall, respectively. Compared to the high latitudes, regions between 40° S and 40° N exhibit a six-month phase shift with the minimum FCO_2' occurring in winter and the maximum in summer. Globally,

coastal seas act as a CO_2 sink all year long with a slightly more intense monthly uptake during spring (-18.9 Tg C month^{-1}) and summer (-21.1 Tg C month^{-1}) while winter and fall each contributes to an equivalent CO_2 uptake flux of -12.5 Tg C month^{-1}. In the open ocean, the more intense CO_2 sink occurs in winter (-195.6 Tg C month^{-1}) followed by fall (-133 Tg C month^{-1}), spring (-122.5 Tg C month^{-1}) and summer (-7 Tg C month^{-1}), respectively.

Global maps of the respective contribution of the different drivers (sea-ice cover, wind speed, ΔpCO_2 and cross-correlation term, β in equation 8) to the total seasonal FCO_2 cycle are presented in Figure 7 (see Figure S1 in supplement for values integrated per MARCATS unit). In order to highlight regions with the highest absolute seasonal variability, the β terms are multiplied by the RMS of the total FCO_2'. Although there is a significant regional variability for the same latitudinal band (i.e. from one MARCATS to another, Figure S1), a strong correlation between the seasonal cycle of FCO_2 and that of ΔpCO_2 is observed for the vast majority of latitudinal zones. Flux and gradient anomalies are in phase ($\beta_{\Delta pCO_2} > 0$) and the high values of $\beta_{\Delta pCO_2}$ demonstrate that changes in ΔpCO_2 explain the majority of the seasonal changes in FCO_2. The correlation between the other terms ($\beta_{sea\text{-}ice}$, β_{wind}, $\beta_{\text{cross-correlation}}$) and FCO_2', in addition to presenting more variable contributions within the same latitudinal band (Figure S1), is more complex than that of ΔpCO_2 and can be either in phase with that of the FCO_2' ($\beta > 0$) in some regions or anti-correlated ($\beta < 0$) in others. For instance, the anomaly associated with the sea-ice cover can either be in phase ($\beta_{sea\text{-}ice} > 0$) or anti-correlated ($\beta_{sea\text{-}ice} < 0$) with FCO_2' depending on whether FCO_2 is a source or a sink of CO_2 for the atmosphere and hence on the pCO_2 gradient. $\beta_{sea\text{-}ice}$ is positive when $\Delta pCO_2 < 0$ and negative when $\Delta pCO_2 > 0$.

Although the grid point and the MARCATS-level analysis reveal significant small-scale spatial variabilities in the β terms, the temporal evolution of the different drivers aggregated by latitudinal bands confirms that the changes in ΔpCO_2 explain most of the seasonal variations of FCO_2 (Figure 8). In some regions (i.e., between 10° - 40° N), ΔpCO_2 explains even all of the FCO_2 variability (superposition between black and red curves in Figure 8) while at latitudes > 40° N, the seasonal ΔpCO_2

variability induces larger anomalies than the total FCO_2', which are compensated by the other drivers as an dampening effect on FCO_2 seasonal variability. Although the effect of the sea-ice cover can be important locally in the Southern hemisphere, it only contributes slightly to the seasonal change in FCO_2 in bands south of 60° S. In the Northern Hemisphere and especially for latitudinal bands > 60° N, the seasonal FCO_2 profile associated with the change of the sea-ice cover is pronounced underlining the important contribution of this driver in this region. Although there are regions where FCO_2' is in phase with the one generated by wind speed such as in the Barents Sea ($\beta_{wind} > 0$), β_{wind} tends to act as a compensating term with respect to other parameters for most latitudinal bands. This is particularly true in the latitudinal band > 60° N, where the FCO_2' seasonal signal is in opposition to the one generated by wind speed. The effect of wind speed on the FCO_2 variability is mainly found in latitudinal band > 40° in both hemispheres. In the other regions, the effect of the wind either intensifies or dampens the magnitude of the FCO_2 seasonality depending on the month, resulting in a negligible net effect except in bands 0° - 10° S where it contributes significantly to the (small) FCO_2 variability. Finally, the contribution of the cross-correlation terms illustrates non-linear interactions between the various drivers and has a negligible effect on the FCO_2 variability in about half of the latitudinal bands. The cross terms are significant only at > 60° S and between 40° N - 60° N. In the latter latitudinal band, however, the contribution of the cross terms to the seasonality of FCO_2 remains lower than that of both ΔpCO_2 and wind speed. Globally, when all of the coastal seas are integrated (bottom panel of Figure 8), the seasonal pattern mostly follows that of the high latitudes with a minimum FCO_2' in summer and a maximum in winter. The $\mathrm{RMS}_{FCO_2'}$ amplitude of the global seasonal profile amounts to a value of 0.1 mol C m^{-2} yr^{-1}. Similarly to latitudes > 40° N, the global seasonal ΔpCO_2 variability induces larger anomalies than the total FCO_2', which are partly compensated by the effect of wind.

3.4 Quantification of uncertainty

In coastal seas, the total uncertainty (σ) varies widely from one MARCATS to another, with values ranging from 0.1 mol C m^{-2} yr^{-1} to 0.8 mol C m^{-2} yr^{-1} (Figure 3 and Table S1). The largest uncertainty is found in areas along the coast of Southwest Africa (MARCATS 24) and values of $\sigma \geq 0.5$ mol C yr^{-1} are

mainly encountered in subpolar margins (MARCATS 1, 5, 11 and 42), EBCs (MARCATS 4, 22, 24), in marginal seas (MARCATS 21, 40, 41) and in the Norwegian Basin of polar margins. In MARCATS 12 (Hudson Bay), 29 (Persian Gulf), 30 (East Arabian Sea) and 31 (Bay of Bengal), most of which are located in the Indian Ocean, σ is low (≤ 0.1 mol m^{-2} yr^{-1}). However, they should be considered with caution since the contribution of the pCO_2 uncertainty (σ_{pCO2}) cannot be calculated due to the absence of observational pCO_2 data in those regions. Globally, for the coastal ocean, the FCO_2 uncertainty amounts to 0.02 Pg C yr^{-1} (~ 10 % of the coastal seas FCO_2, Table 1). In all MARCATS, the uncertainty associated to the pCO_2 field is the largest and the global σ_{pCO2} amounts to 0.017 Pg C yr^{-1} for coastal regions. A similar pattern is found in the open ocean, where σ_{pCO2} is the main source of uncertainty with a global value of 0.23 Pg C yr^{-1} to be compared with the total uncertainty of 0.26 Pg C yr^{-1} for the open ocean (Table 1). Both in coastal seas and the open ocean, the choice of the k_{660}-formulation (σ_k) yields a relative uncertainty of 7 %. The uncertainty associated to wind speed (σ_{wind}) however reveals a more complex spatial pattern. On the coastal seas, σ_{wind} is low when integrated globally (0,003 Pg C yr^{-1}, corresponding to 4 % difference between FCO_2 obtained using the three wind products) but can be as large as 16 % and 12 % in marginal seas and in the Indian basin, respectively. In agreement with the study of Roobaert et al. (2018), the effect associated with the choice of the wind product is more important for the open ocean than for coastal seas with an uncertainty of 12 % globally (σ_{wind} value of 0.090 Pg C yr^{-1}) with the largest uncertainties in the Pacific basin and in the Southern ocean. Because of the temporal heterogeneity of the data coverage in coastal regions, the resulting FCO_2 uncertainty also varies along the year and not only spatially (Figure 5). In all latitudinal bands, 75 % of the monthly uncertainty is below 0.25 mol m^{-2} yr^{-1} with the exception of the band between 40° S and 60° S as a consequence of a much lower pCO_2 observational data coverage. Even in this last region, the amplitude of the seasonal uncertainty does not exceed that of FCO_2.

4 Discussion

4.1 Annual mean fluxes

The global annual mean coastal CO_2 sink of -195 Tg C yr^{-1} (-0.20 Pg C yr^{-1}) generated by our calculation falls at the low end of the range of past estimates spanning from -0.45 Pg C yr^{-1} to -0.21 Pg C yr^{-1} (Borges, 2005; Borges et al., 2005; Cai et al., 2006; Chen et al., 2013; Chen & Borges, 2009; Dai et al., 2013; Laruelle et al., 2010). This confirms that previous estimates based on sparse datasets likely overestimated the uptake of CO_2 by the coastal seas because of the inherent biases associated to the extrapolation of a limited number of local estimates to large scales and an over-representation of temperate and sub-polar systems, which are mostly CO_2 sinks. Support for this interpretation comes from the fact that our estimate agrees very well with that of Laruelle et al. (2014) (-192 Tg C yr^{-1}), who upscaled 3 million local measurements using different regional integration methods depending on the data density, also accounting for differences in the coastal seas delimitation and taking into consideration the sea-ice cover in the FCO_2 calculations. Our study improves upon that of Laruelle et al. (2014) thanks to our continuous spatial and temporal coverage of FCO_2 estimates for all the coastal seas at 0.25° resolution as opposed to Laruelle et al. (2014) who calculated 150 regional FCO_2 estimates using the COSCAT/MARCATS segmentation (Laruelle et al., 2013). Taken that the work of Laruelle et al. (2014) is the most comprehensive, spatially resolved study to date and relies on the same spatial definition of the coastal regions as the one used in our study, we perform a comparison at the level of each MARCATS (Figure S2a and Table S1 in the supplementary information). Furthermore, the general spatial trends observed in our work and in Laruelle et al. (2014) such as the latitudinal profile of FCO_2 are also consistent with several earlier studies (Borges et al., 2005; Cai, 2011; Chen et al., 2013; Chen & Borges, 2009; Laruelle et al., 2010). The role of high latitude shelves as efficient CO_2 sinks as a consequence of their low water temperatures has also been evidenced by numerous studies on the Arctic ocean (Bates & Mathis, 2009). We do not emphasize the comparison for MARCATS 4 (Peruvian upwelling), 22 (Moroccan upwelling) and 27 (West Arabian Sea) due to the low performance of the neural network technique in these regions (see sections 3.1 and 3.2). In general, the absolute magnitude of sources and sinks are slightly lower in our calculations than in Laruelle et al. (2014), but both studies are in relatively good agreement overall. All MARCATS in polar and subpolar margins act as a CO_2

sink for both studies. In tropical margins, EBCs and WBCs, the sign (a sink or a source) of FCO_2 is also in agreement except for one or two MARCATS in each category (i.e., MARCATS 23, 38, 6 and 19). Along the Indian margins, i.e., regions where FCO_2 values calculated by Laruelle et al. (2014) have a low degree of confidence, our results show FCO_2 values with opposite signs for all of the MARCATS with the exception of the East Arabian Sea (MARCATS 30). In addition, out of the 9 MARCATS located in marginal seas, only two display FCO_2 with the same sign. In quantitative terms, a difference of less than 1 mol C m^{-2} yr^{-1} is observed between the two studies in all MARCATS except for two regions (MARCATS 40 and 41) contributing to merely 4 % of the total surface area of the coastal regions. These two regions have a low degree of confidence in the study of Laruelle et al. (2014).

We also compare our results to those of Bourgeois et al. (2016) which were calculated using the Oceanic General Circulation Model (OGCM) NEMO-PISCES (Nucleus for European Modelling of the Ocean - Pelagic Interaction Scheme for Carbon and Ecosystem Studies). Overall, the two studies are in relatively good agreement regarding the FCO_2 sign (33 over 45 MARCATS), but FCO_2 values modelled by Bourgeois et al. (2016) produce more intense CO_2 sinks and weaker sources (Figure S2b and Table S1). Out of the 45 MARCATS, only 13 present differences exceeding 1 mol C m^{-2} yr^{-1}, corresponding to a global coastal surface area of ~ 30 %. These differences are mainly located on narrow shelves, which are poorly resolved by OGCMs (Bourgeois et al., 2016) and in descending order, are located in marginal seas, EBCs and WBCs, and subpolar and polar regions. A difference greater than 2 mol C m^{-2} yr^{-1} is observed only in the Black Sea.

4.2 CO_2 flux densities

Both in the open and coastal ocean, several processes and their interactions govern the direction and intensity of the CO_2 exchange with the atmosphere. These processes range from physical (i.e., solubility, mixing and upwelling waters) to biological (i.e. primary production). Moreover, the supply of carbon and nutrients by rivers from continents may also affect the dynamics of the air-sea exchange in coastal regions. Due to the comparatively high photosynthetic carbon fixation and biological activity that occur in coastal regions in comparison to the rest of the ocean, past observational (Borges et al.,

2005; Cai, 2011; Chen et al., 2013; Dai et al., 2013; Laruelle et al., 2010, 2014, 2018) and modelling (Andersson & Mackenzie, 2004; Mackenzie et al., 2012) studies suggest that the FCO_2 dynamics substantially differ between the coastal regions and the adjacent open ocean basins. In particular, past studies have estimated that the global mean air-sea CO_2 exchange rates for coastal seas vary between -0.7 mol C m^{-2} yr^{-1} and -1.2 mol C m^{-2} yr^{-1} implying that, globally, they act as a more efficient CO_2 sink than the open ocean per unit surface area (i.e., -0.36 mol C m^{-2} yr^{-1} in Takahashi et al., 2009). In this study, we observe a difference of 36 % between the global mean FCO_2 for the coastal seas (-0.58 mol C m^{-2} yr^{-1}) and that for the open ocean (-0.37 mol C m^{-2} yr^{-1}). However, our analysis of the FCO_2 maps (Figure 2) as well as their latitudinal profiles (Figure 4) reveal that there is little difference between these two systems when compared by latitude. The FCO_2 distributions for coastal and the open ocean are relatively similar with CO_2 sinks at temperate and high latitudes and sources or values close to equilibrium along the Tropics and the Equator. This general latitudinal trend for coastal regions which has been suggested by previous studies (i.e., Borges et al., 2005; Cai, 2011; Chen et al., 2013; Laruelle et al., 2010, 2014) has now become very clear.

The main difference between the coastal and the open ocean consists of the width of the latitudinal band where the open ocean acts as a source (Figure 4), which is narrower (15° N - 15° S) than that of the coastal seas (30° N - 20° S). Our results also reveal larger differences between the two systems locally, in particular in river-dominated coastal regions. The impact of riverine inputs on the coastal CO_2 flux, for instance, was investigated by Lefèvre et al. (2010) for the Amazon plume, which acts as a CO_2 sink while the adjacent ocean is a source . Taken this remarkable similarity in CO_2 flux densities, our results thus suggest that most of the difference in the global mean FCO_2 between coastal and the open ocean stems from the differing areal distribution of the coastal regions, which are much more abundant in the high latitude of the Northern Hemisphere where intense CO_2 sinks take place. Indeed, the coastal seas located in areas > 60° N (25 % of the total surface coastal area against only 1 % for the open ocean) take up more than one-third of the global coastal uptake flux (-98 Tg C yr^{-1}). This disproportionate contribution to the global coastal CO_2 sink is consistent with earlier works (Cai, 2011; Laruelle et al.,

2010, 2014). Excluding regions located above 60° N, the global mean FCO_2 obtained for coastal seas is -0.39 mol C m^{-2} yr^{-1}, remarkably close to -0.35 mol C m^{-2} yr^{-1} for the open ocean. This similarity between coastal regions and the open ocean was also suggested by the work of Bourgeois et al. (2016) in their modeling study as well as by Wanninkhof et al. (2013). In the latter, the integrated coastal FCO_2 estimate (-0.18 Pg C yr^{-1}) was calculated by extrapolation assuming that the FCO_2 of the coastal seas per unit area is the same as that of the adjacent ocean. With the exception of the local discrepancies mentioned above (river plume, estuary mouth, …), the surprisingly similar latitudinal distribution of flux densities between the coast and the adjacent open ocean observed in this study suggests that, in addition to others factor explaining the spatial heterogeneity, the thermal effect is the main driver that governs the zonal latitudinal pattern of sources and sinks for the ocean as a whole. This effect translates into a change in CO_2 solubility via the term K_0 in equation 1. Cooling/warming waters in high/low latitudes induce an increase/decrease in the CO_2 solubility and, thus, a lower/higher pCO_2 in the surface seawater. The dominance of this process that was suggested by Gruber (2015) when commenting on the results of Laruelle et al. (2014) can now be quantified thanks to our analysis.

4.3 Global Ocean CO_2 budget

Globally, our net ocean carbon uptake of -1.7 ± 0.3 Pg C yr^{-1} (coastal and open ocean) represents the sum of a net uptake of anthropogenic CO_2, a net exchange flux of natural carbon in response to climate variability and change, plus an outgassing of river-derived carbon. If we assume a pre-industrial river outgassing rate of 0.45 ± 0.18 Pg C yr^{-1} (Jacobson et al., 2007) and an outgassing flux of natural CO_2 of the order of 0.4 ± 0.2 Pg C yr^{-1} (Gruber et al., 2019), our estimates implies an anthropogenic CO_2 uptake rate of -2.6 ± 0.4 Pg C yr^{-1} for the 1998 through 2015 period. This uptake estimate is statistically identical to that recently estimated by Gruber et al. (2019) (-2.6 ± 0.3 Pg C yr^{-1}) on the basis of ocean interior changes in anthropogenic CO_2 between 1994 and 2007. It is also consistent with other independent estimates, such as those based on an Green's function ocean inversion method (-2.4 Pg C yr^{-1}; Gruber et al., 2009, adjusted to the year 2007), those based on an inverse model (-2.6 Pg C yr^{-1}; DeVries, 2014), or those based on a compilation of models and observations (-2.0 ± 0.6 Pg C yr^{-1},

Wanninkhof et al. 2013). The anthropogenic CO_2 uptake estimated here would reaches -2.9 ± 0.5 Pg C yr^{-1} when considering the revisited global pre-industrial river carbon flux (0.78 ± 0.41 Pg C yr^{-1}) proposed by Resplandy et al. (2018). While the magnitude of global ocean carbon uptake estimates have not changed much in recent years, the uncertainty of our estimate as well as that for the open ocean has decreased over time. While Laruelle et al. (2014) reported an uncertainty of 0.05 Pg C yr^{-1} for the global coastal ocean, our estimate is now 0.02 Pg C yr^{-1}. Similarly, the uncertainty estimate for the global open ocean of 0.26 Pg C yr^{-1} is halved relative to the initial estimate by Landschützer et al. (2014) of 0.53 Pg C yr^{-1}. This reduction is the result of (1) improved data coverage and (2) improved analysis methods. Note that the influence of regional biases is not taken into account in the calculation of the FCO_2 uncertainty in this study. However, considering that the globally averaged bias is null and that most regional biases are much lower than θ_{obs} (Laruelle et al., 2017), including them into the uncertainty calculation would likely only marginally increase it.

Our analysis reveals that, both for the coastal regions and the open ocean, most of the uncertainty over the FCO_2 comes from uncertainties associated to the pCO_2 products themselves. This can be attributed to the existence of large areas that remain undersampled in spite of the international community effort to integrate more quality controlled data in the yearly releases of databases such as SOCAT (Bakker et al., 2016). Although most of the world's ocean is now relatively well monitored and simulated by the SOM-FFN derived data products of Landschützer et al. (2014) or Laruelle et al. (2017), some of the least sampled regions represent a challenge even for the best interpolation algorithm because their training relies on too small datasets which do not allow fully capturing the biogeochemical dynamics of the region. This likely explains, for example, the poor representation of the Peruvian upwelling by the coastal pCO_2 product of Laruelle et al. (2017), which was thus removed from our regional analysis. Finally, another potential limitation of our calculations is the use of the Atmospheric Boundary Layer to generate the atmospheric pCO_2 field used to calculate the air-water pCO_2 gradient. Recent local studies of coastal environment have suggested that, because of their proximity with continents where anthropogenic sources of CO_2 are taking place, coastal region might be exposed to slightly higher

atmospheric pCO_2 than the oceanic average. In order to quantify the potential effect of such bias, our calculations for the global coastal CO_2 sink were also performed with an atmospheric pCO_2 increased by 2 µatm in the 23° N - 66° N latitudinal band (where most of the Earth landmasses are located), by 1 µatm in the rest of the Northern Hemisphere and by 0.5 µatm in the Southern Hemisphere. The resulting global CO_2 uptake from coastal regions amounts to -207 Tg C yr^{-1}, a 6 % increase in magnitude compared to our initial estimate. This relatively small difference (falling within our uncertainty range) might be better accounted for in future calculations with the use of spatially resolved dry air mixing ratio of CO_2 dataset such as NASA's Goddard Earth Observing System (GEOS) model, or CarbonTracker.

4.4 Seasonal variability

The analysis of the relative contributions of the different drivers to the FCO_2 seasonal variability reveals that, for most regions, the seasonal cycle of FCO_2 is intimately linked to that of ΔpCO_2 (Figures 7a and 8). Although the contribution of ΔpCO_2 is the main driving force of the seasonal variability of FCO_2 in the different latitudinal bands ($\beta_{\Delta pCO_2} > 0$), the contribution of the sea-ice cover and wind speed to the seasonal FCO_2 variability can be large locally, in particular at temperate and high latitudes (Figures 7 and 8). This observation was already reported by Yasunaka et al. (2016) for the Greenland, Barents and Chuchki Seas. In the Northern Hemisphere where most of the coastal seas act as a CO_2 sink, the positive $\beta_{sea\text{-}ice}$ values can be explained by low summer pCO_2 combined with low sea-ice cover pushing FCO_2 toward a stronger sink while in winter, when pCO_2 is high, the sea-ice cover limits this exchange and induces a FCO_2 going towards a weaker sink. The effect of the wind tends to counteract the other two mechanisms ($\beta_{\mathrm{wind}} < 0$). In winter, the wind speed is faster compared to summer and the turbulence at the air-sea interface is increased accordingly. This effect favors the CO_2 exchange (stronger sink) in winter while in summer the wind speed slows down and thereby limits the exchange (weaker sink). The opposite effect of the wind speed with respect to sea-ice and ΔpCO_2 has already been observed for the Barents Sea by Nakaoka et al. (2006).

All in all, a very strong seasonal variability is observed at higher latitudes, a smaller one between 40° S and 40° N and a very low one between 10° N and 10° S. The global FCO_2 seasonal profile for all of the coastal seas mostly follows that observed for high latitudes (bottom panel of Figure 8). As was the case for the CO_2 flux density analysis, this trend reflects that the coastal seas located at high latitudes influence greatly the global seasonal FCO_2 profile as a result of their disproportionate contribution to the global uptake. Because ΔpCO_2 is the major driver for all latitudinal bands and due to the six-months shift in the phase of the seasonal profile between low and high latitudes, the amplitude of the global FCO_2 seasonal cycle is dampened and is of the same order of magnitude as that of the equatorial regions. As a result of the uneven areal surface distribution of the coastal seas at high latitudes in the Northern Hemisphere and their large contribution to the global seasonal profile, the more intense CO_2 uptake is encountered in summer globally while this is observed in winter in the open ocean (Landschützer et al., 2018).

5 Concluding remarks and directions for future research

Up until now, the dynamics of the CO_2 exchange at the air-sea interface in coastal regions remained poorly understood and its quantification stayed tainted with large uncertainties. With a better spatial and temporal coverage of observational data, our study provides a better constrained coastal FCO_2 globally and regionally using the MARCATS segmentation. We produce, for the first time, monthly FCO_2 maps for the coastal sea regions worldwide at a high spatial resolution of 0.25 degree using the recent coastal pCO_2 product of Laruelle et al. (2017) derived from a two-step artificial neural network for the 1998-2015 period.

Although this study allows us to analyze the climatological FCO_2 seasonality and to quantify the respective contributions of ΔpCO_2, wind speed and sea-ice cover to the seasonal signal, the roles of processes indirectly affecting the seasonality of FCO_2 through their effect on pCO_2 in surface coastal waters remains largely unknown. For instance, changes in *SST* and *SSS* induce variations in pCO_2 by

physico-chemical processes that impact the CO_2 exchange. Similarly, variations in alkalinity (*ALK*) and dissolved inorganic carbon (*DIC*) governed by biogeochemical and physical processes can also control the seasonality of pCO_2. In the study of Laruelle et al. (2017), the effect on pCO_2 seasonality associated with changes in *SST* was quantified and compared to non-thermal effects for different oceanic basins and at global scale. This study emphasizes that the solubility pump is the dominant process in the seasonality of pCO_2 for all latitudinal bands in spite of differences between oceanic basins, a result consistent with past studies (i.e., Laruelle et al., 2014; Shadwick et al., 2010). However, their study also highlights that the thermal component alone cannot explain the entirety of the pCO_2 seasonal cycle and that non-thermal processes (i.e., biological uptake, mixing…) also contribute significantly to the seasonal variation of pCO_2, especially in temperate regions. At high latitudes > 60° in both hemispheres, high/low pCO_2 values are observed during winter/summer in this study confirming that the solubility pump is not the dominant process governing the pCO_2 seasonal variability in these regions.

The use of ocean biogeochemical models allows one to further disentangle the respective effects of *ALK*, *DIC*, *SSS* and *SST* on the seasonal variability of pCO_2 and to identify the contributions of physical, biological and mixing processes to variations in the pCO_2 field. Such studies have been conducted along the California current along the west coast of the United States (Turi et al., 2014) as well as in four different shelf seas (South and Southeast Brazilian shelves, Uruguayan and Patagonia shelves) along the southwestern Atlantic ocean (Arruda et al., 2015). Both studies concluded that *SST* (the solubility pump) and *DIC* associated to water circulation and the biological pump are the main drivers of seasonality but that their effects on pCO_2 changes can counteract one another. In the California current, the water circulation generated by the strong upwelling is the main control of the pCO_2 seasonality, which is further influenced by the solubility and biological pumps. In the study of Arruda et al. (2015) on the Patagonia shelf, the opposite is observed and the solubility and biological pumps govern the seasonality of pCO_2 with only a small contribution from the water circulation. These different contributions to the pCO_2 seasonal variability remain however unknown at the global scale as

in coastal seas not under upwelling influence. Although they can only be estimated through Ocean Biogeochemical models, our data based coastal CO_2 climatology at high spatial and temporal resolution provide the necessary observational constraints against which these models can be evaluated. A complete attribution analysis of the FCO_2 seasonality on the global coastal regions is thus a goal that should be reachable in the near future. Moreover, long-term trends and the interannual variability of global coastal CO_2 fluxes still remain poorly constrained (Laruelle et al., 2018). Coastal regions are subject to large interannual variations (IAV) driven by riverine loading changes or climatic events such as El Nino cycle. The analysis of the coastal FCO_2 IAV, its environmental controls and how it may impact seasonal cycle should be investigated in future research. Some attention should also be paid to the potential effects of changes in others environmental parameters (i.e., expected changes in wind speed and pattern, decrease of the sea-ice cover or increase in atmospheric pCO_2) on the spatio-temporal FCO_2 trend. Such investigations have already been carried out for the open ocean but are still missing in coastal seas at global scale. For instance, the increase in atmospheric pCO_2 in addition to increasing surface water pCO_2, tends to enhance the amplitude of the seasonal signal in FCO_2 (Landschützer et al., 2018). The study of Wanninkhof & Trinanes (2017) also suggests that the observed increase in wind speed does not affect the air-sea exchange homogeneously in the ocean worldwide and depends on the patterns and the localization of this wind speed changes. One could thus speculate that similar effect will be observed in the coastal ocean but future research is still needed to properly decipher to complex dynamics of FCO_2 in the coastal ocean and should be included in ongoing investigations of the global carbon budget. Our study provides the necessary ground work for such future research. In parallel, the ongoing community effort to better represent the least monitored coastal regions in SOCAT will further help reducing the uncertainties associated to the pCO_2 field and a better representation of the spatial patterns of atmospheric pCO_2 will contribute to even better constrained FCO_2 estimates as well.

Acknowledgments, Samples, and Data

The observation-based global monthly gridded sea-surface pCO_2 products are provided for the coastal seas by Laruelle et al. (2017) and for the open ocean by Landschützer et al. (2017). They are accessible

on the Biogeosciences journal website (https://doi.org/10.5194/bg-14-4545-2017) and on the NOAA website (https://www.nodc.noaa.gov/ocads/oceans/SPCO2_1982_2015_ETH_SOM_FFN.html) respectively. The atmospheric partial pressure of CO_2 is provided by the NOAA Marine Boundary layer and can be found on their website (https://www.esrl.noaa.gov/gmd/ccgg/mbl/). The 6 hours 0.25 degree global atmospheric reanalysis ERA-Interim wind product dataset (Dee et al., 2011) can be downloaded on the European Centre for Medium-Range Weather Forecasts (ECMWF) website. The NOAA High-resolution sea surface temperature (Reynolds et al., 2007) and sea-ice cover (Cavalieri et al., 1996; Grumbine, 1996; Reynolds et al., 2007) data are provided by the NOAA/OAR/ESRL PSD, Boulder, Colorado, USA, from their website at https://www.esrl.noaa.gov/psd/. The daily EN4 sea surface salinity (Good et al., 2013) can be found on the Met Office Hadley center website. The authors declare that they have no conflict of interest. AR is funded by a teaching assistantship grant awarded by the Université Libre de Bruxelles (ULB). GL has been supported by Labex L-IPSL LP3 SP3, which is funded by ANR (Grant #ANR-10-LABX-0018) and is now research associate of the F.R.S.-FNRS at the ULB. PR received funding from the VERIFY project from the European Union's Horizon 2020 research and innovation program under grant agreement No. 776810. PL is supported by the Max Planck Society for the Advancement of Science. NG acknowledges support from ETH Zürich and the Swiss National Science Foundation through the XEBUS project (200020_175787). The authors thank Adam Hastie for his technical support with the GIS-based coastal seas MARCATS delimitation used in this study.

References

Andersson, A. J., & Mackenzie, F. T. (2004). Shallow-water oceans: a source or sink of atmospheric CO_2? *Frontiers in Ecology and the Environment*, *2*(7), 348–353.

Arruda, R., Calil, P. H. R., Bianchi, A. A., Doney, S. C., Gruber, N., Lima, I., & Turi, G. (2015). Air-sea CO_2 fluxes and the controls on ocean surface pCO_2 seasonal variability in the coastal and open-ocean southwestern Atlantic Ocean: a modeling study. *Biogeosciences*, *12*, 5793–5809. https://doi.org/10.5194/bg-12-5793-2015

Atlas, R., Hoffman, R. N., Ardizzone, J., Leidner, S. M., Jusem, J. C., Smith, D. K., & Gombos, D. (2011). A cross-calibrated, multiplatform ocean surface wind velocity product for meteorological and oceanographic applications. *Bulletin of the American Meteorological Society*, *92*(2), 157–174. https://doi.org/10.1175/2010BAMS2946.1

Bakker, D. C. E., Pfeil, B., Landa, C. S., Metzl, N., O'Brien, K. M., Olsen, A., et al. (2016). A multi-decade record of high-quality fCO_2 data in version 3 of the Surface Ocean CO_2 Atlas (SOCAT). *Search.Proquest.Com*, *8*, 383–413. https://doi.org/doi:10.5194/essd-8-383-2016

Bates, N. R., & Mathis, J. T. (2009). The Arctic Ocean marine carbon cycle: Evaluation of air-sea CO_2 exchanges, ocean acidification impacts and potential feedbacks. *Biogeosciences*, *6*(11), 2433–2459. https://doi.org/10.5194/bg-6-2433-2009

Bauer, J. E., Cai, W., Raymond, P. A., Bianchi, T. S., Hopkinson, C. S., & Regnier, P. A. (2013). The changing carbon cycle of the coastal ocean. *Nature*, *504*(7478), 61. https://doi.org/10.1038/nature12857

Borges, A. V. (2005). Do we have enough pieces of the jigsaw to integrate CO_2 fluxes in the coastal ocean? *Estuaries*, *28*(1), 3–27. https://doi.org/10.1007/BF02732750

Borges, A. V., Delille, B., & Frankignoulle, M. (2005). Budgeting sinks and sources of CO_2 in the coastal ocean: Diversity of ecosystem counts. *Geophysical Research Letters*, *32*(14), 1–4. https://doi.org/10.1029/2005GL023053

Bourgeois, T., Orr, J. C., Resplandy, L., Terhaar, J., Ethé, C., Gehlen, M., & Bopp, L. (2016). Coastal-ocean uptake of anthropogenic carbon. *Biogeosciences*, *13*(14), 4167–4185. https://doi.org/10.5194/bg-13-4167-2016

Cai, W. (2011). Estuarine and Coastal Ocean Carbon Paradox: CO_2 Sinks or Sites of Terrestrial Carbon Incineration? *Annual Review of Marine Science*, *3*(1), 123–145. https://doi.org/10.1146/annurev-marine-120709-142723

Cai, W., Dai, M., & Wang, Y. (2006). Air-sea exchange of carbon dioxide in ocean margins: A province-based synthesis. *Geophysical Research Letters*, *33*(12), 2–5. https://doi.org/10.1029/2006GL026219

Cavalieri, D., Parkinson, C., Gloersen, P., & Zwally, H. J. (1996). Sea ice concentrations from Nimbus-7 SMMR and DMSP SSM/I passive microwave data. National Snow and Ice Data Center, Boulder, Colorado. Digital media.

Chen, C. T. A., & Borges, A. V. (2009). Reconciling opposing views on carbon cycling in the coastal ocean: Continental shelves as sinks and near-shore ecosystems as sources of atmospheric CO_2. *Deep Sea Research Part II: Topical Studies in Oceanography*, *56*(8–10), 578–590. https://doi.org/10.1016/j.dsr2.2009.01.001

Chen, C. T. A., Huang, T. H., Chen, Y. C., Bai, Y., He, X., & Kang, Y. (2013). Air-sea exchanges of CO_2 in the world's coastal seas. *Biogeosciences*, *10*(10), 6509–6544. https://doi.org/10.5194/bg-10-6509-2013

Couldrey, M. P., Oliver, K. I. C., Yool, A., Halloran, P. R., & Achterberg, E. P. (2016). On which timescales do gas transfer velocities control North Atlantic CO_2 flux variability? *Global Biogeochemical Cycles*, *30*(5), 787–802. https://doi.org/10.1002/2015GB005267

Dai, M., Cao, Z., Guo, X., Zhai, W., Liu, Z., Yin, Z., et al. (2013). Why are some marginal seas sources of atmospheric CO_2? *Geophysical Research Letters*, *40*(10), 2154–2158. https://doi.org/10.1002/grl.50390

Deacon, E. L. (1977). Gas transfer to and across an air-water interface. *Tellus*, *29*(4), 363–374. https://doi.org/10.1111/j.2153-3490.1977.tb00724.x

Dee, D. P., Uppala, S. M., Simmons, A. J., Berrisford, P., Poli, P., Kobayashi, S., et al. (2011). The ERA-Interim reanalysis: Configuration and performance of the data assimilation system. *Quarterly Journal of the Royal Meteorological Society*, *137*(656), 553–597. https://doi.org/10.1002/qj.828

DeVries, T. (2014). The oceanic anthropogenic CO_2 sink: Storage, air-sea fluxes, and transports over the industrial era. *Global Biogeochemical Cycles*, *28*(7), 631–647. https://doi.org/10.1002/2013GB004739

Doney, S. C., Lima, I., Feely, R. A., Glover, D. M., Lindsay, K., Mahowald, N., et al. (2009). Mechanisms governing interannual variability in upper-ocean inorganic carbon system and air–sea CO_2 fluxes: Physical climate and atmospheric dust. *Deep Sea Research Part II: Topical Studies in Oceanography*, *56*(8–10), 640–655. https://doi.org/10.1016/j.dsr2.2008.12.006

Etcheto, J., & Merlivat, L. (1988). Satellite determination of the carbon dioxide exchange coefficient at the ocean-atmosphere interface: A first step. *Journal of Geophysical Research: Oceans*, *93*(C12), 15669. https://doi.org/10.1029/JC093iC12p15669

Frankignoulle, M., & Borges, A. V. (2001). European continental shelf as a significant sink for atmospheric carbon dioxide. *Global Biogeochemical Cycles*, *15*(3), 569–576.

Friederich, G. E., Ledesma, J., Ulloa, O., & Chavez, F. P. (2008). Air-sea carbon dioxide fluxes in the coastal southeastern tropical Pacific. *Progress in Oceanography*, *79*(2–4), 156–166. https://doi.org/10.1016/j.pocean.2008.10.001

Good, S. A., Martin, M. J., & Rayner, N. A. (2013). EN4: Quality controlled ocean temperature and salinity profiles and monthly objective analyses with uncertainty estimates. *Journal of Geophysical Research: Oceans*, *118*(12), 6704–6716. https://doi.org/10.1002/2013JC009067

Gruber, N. (2015). Ocean biogeochemistry: Carbon at the coastal interface. *Nature*. https://doi.org/10.1038/nature14082

Gruber, N., Gloor, M., Mikaloff Fletcher, S. E., Doney, S. C., Dutkiewicz, S., Follows, M. J., et al. (2009). Oceanic sources, sinks, and transport of atmospheric CO_2. *Global Biogeochemical Cycles*, *23*(1), 1–21. https://doi.org/10.1029/2008GB003349

Gruber, N., Clement, D., Carter, B. R., Feely, R. A., Van Heuven, S., Hoppema, M., et al. (2019). The oceanic sink for anthropogenic CO_2 from 1994 to 2007. *Science*, *363*(6432), 1193–1199. https://doi.org/10.1126/science.aau5153

Grumbine, R. W. (1996). Automated passive microwave sea ice concentration analysis at NCEP. *NOAA Tech. Note*, *120*, 1–13.

Ho, D. T., Wanninkhof, R., Schlosser, P., Ullman, D. S., Hebert, D., & Sullivan, K. F. (2011). Toward a universal relationship between wind speed and gas exchange: Gas transfer velocities measured with 3He/SF6 during the Southern Ocean Gas Exchange Experiment. *Journal of Geophysical Research: Oceans*, *116*(7), C00F04.

https://doi.org/10.1029/2010JC006854

Jacobs, C. M. J., Kohsiek, W., & Oost, W. A. (1999). Air-sea fluxes and transfer velocity of CO_2 over the north sea: Results from ASGAMAGE. *Tellus, Series B: Chemical and Physical Meteorology*, *51*(3), 629–641. https://doi.org/10.1034/j.1600-0889.1999.t01-2-00005.x

Jacobson, A. R., Fletcher, S. E. M., Gruber, N., Sarmiento, J. L., & Gloor, M. (2007). A joint atmosphere-ocean inversion for surface fluxes of carbon dioxide: 1. Methods and global-scale fluxes. *Global Biogeochemical Cycles*, *21*(1). https://doi.org/10.1029/2005GB002556

Kalnay, E., Kanamitsu, M., Kistler, R., Collins, W., Deaven, D., Gandin, L., et al. (1996). The NCEP/NCAR 40-year reanalysis project. *Bulletin of the American Meteorological Society*, *77*(3), 437–471. https://doi.org/10.1175/1520-0477(1996)077<0437:TNYRP>2.0.CO;2

Kanamitsu, M., Ebisuzaki, W., Woollen, J., Yang, S. K., Hnilo, J. J., Fiorino, M., & Potter, G. L. (2002). NCEP-DOE AMIP-II reanalysis (R-2). *Bulletin of the American Meteorological Society*, *83*(11), 1631-1643+1559. https://doi.org/10.1175/BAMS-83-11-1631

Keeling, R. F., & Manning, A. C. (2014). Studies of Recent Changes in Atmospheric O_2 Content. In *Treatise on Geochemistry (Second Edition)* (pp. 385–404). https://doi.org/http://dx.doi.org/10.1016/B978-0-08-095975-7.00420-4

Kuss, J., Nagel, K., & Schneider, B. (2004). Evidence from the Baltic Sea for an enhanced CO_2 air-sea transfer velocity. *Tellus, Series B: Chemical and Physical Meteorology*, *56*(2), 175–182. https://doi.org/10.1111/j.1600-0889.2004.00092.x

Landschützer, P., Gruber, N., Bakker, D. C. E., Schuster, U., Nakaoka, S., Payne, M. R., et al. (2013). A neural network-based estimate of the seasonal to inter-annual variability of the Atlantic Ocean carbon sink. *Biogeosciences*, *10*(11), 7793–7815. https://doi.org/10.5194/bg-10-7793-2013

Landschützer, P., Gruber, N., Bakker, D. C. E., & Schuster, U. (2014). Recent variability of the global ocean carbon sink. *Global Biogeochemical Cycles*, *28*(9), 927–949. https://doi.org/10.1002/2014GB004853

Landschützer, P., Gruber, N., & Bakker, D. C. E. (2016). Decadal variations and trends of the global ocean carbon sink. *Global Biogeochemical Cycles*, *30*(10), 1396–1417. https://doi.org/10.1002/2015GB005359

Landschützer, P., Gruber, N., & Bakker, D. C. E. (2017). An updated observation-based global monthly gridded sea surface pCO_2 and air-sea CO_2 flux product from 1982 through 2015 and its monthly climatology (NCEI Accession 0160558). Version 2.2. NOAA National Centers for Environmental Information. Dataset.

Landschützer, P., Gruber, N., Bakker, D. C. E., Stemmler, I., & Six, K. D. (2018). Strengthening seasonal marine CO_2 variations due to increasing atmospheric CO_2. *Nature Climate Change*. https://doi.org/10.1038/s41558-017-0057-x

Laruelle, G. G., Dürr, H. H., Slomp, C. P., & Borges, A. V. (2010). Evaluation of sinks and sources of CO_2 in the global coastal ocean using a spatially-explicit typology of estuaries and continental shelves. *Geophysical Research Letters*, *37*(15), 1–6. https://doi.org/10.1029/2010GL043691

Laruelle, G. G., Dürr, H. H., Lauerwald, R., Hartmann, J., Slomp, C. P., Goossens, N., & Regnier, P. (2013). Global multi-scale segmentation of continental and coastal waters from the watersheds to the continental margins. *Hydrology and Earth System Sciences*, *17*(5), 2029–2051. https://doi.org/10.5194/hess-17-2029-2013

Laruelle, G. G., Lauerwald, R., Pfeil, B., & Regnier, P. (2014). Regionalized global budget of the CO_2 exchange at the air-water interface in continental shelf seas. *Global Biogeochemical Cycles*, *28*, 1199–1214. https://doi.org/10.1002/2014GB004832

Laruelle, G. G., Landschützer, P., Gruber, N., Tison, J. L., Delille, B., & Regnier, P. (2017). Global high-resolution monthly pCO_2 climatology for the coastal ocean derived from neural network interpolation. *Biogeosciences*, *14*(19), 4545–4561. https://doi.org/10.5194/bg-14-4545-2017

Laruelle, G. G., Cai, W.-J., Hu, X., Gruber, N., Mackenzie, F. T., & Regnier, P. (2018). Continental shelves as a variable but increasing global sink for atmospheric carbon dioxide. *Nature Communications*, *9*(1), 454. https://doi.org/10.1038/s41467-017-02738-z

Lefèvre, N., Diverrès, D., & Gallois, F. (2010). Origin of CO_2 undersaturation in the western tropical Atlantic. *Tellus, Series B: Chemical and Physical Meteorology*, *62*(5). https://doi.org/10.1111/j.1600-0889.2010.00475.x

Liu, K. K., Atkinson, L., Quiñones, R., & Talaue-McManus, L. (2010). *Carbon and Nutrient Fluxes in Continental Margins*.

Springer Science & Business Media. https://doi.org/10.1007/978-3-540-92735-8

Mackenzie, F. T., De Carlo, E. H., & Lerman, A. (2012). Coupled C, N, P, and O Biogeochemical Cycling at the Land-Ocean Interface. In *Treatise on Estuarine and Coastal Science* (Vol. 5, pp. 317–342). https://doi.org/10.1016/B978-0-12-374711-2.00512-X

Manning, A. C., & Keeling, R. F. (2006). Global oceanic and land biotic carbon sinks from the scripps atmospheric oxygen flask sampling network. *Tellus, Series B: Chemical and Physical Meteorology*, *58*(2), 95–116. https://doi.org/10.1111/j.1600-0889.2006.00175.x

Nakaoka, S. I., Aoki, S., Nakazawa, T., Hashida, G., Morimoto, S., Yamanouchi, T., & Yoshikawa-Inoue, H. (2006). Temporal and spatial variations of oceanic pCO_2 and air-sea CO_2 flux in the Greenland Sea and the Barents Sea. *Tellus, Series B: Chemical and Physical Meteorology*, *58*(2), 148–161. https://doi.org/10.1111/j.1600-0889.2006.00178.x

Nightingale, P., Malin, G., Law, C. S., Watson, A. J., Liss, P. S., Liddicoat, M. I., et al. (2000). In situ evaluation of air-sea gas exchange parameterizations using novel conservative and volatile tracers. *Global Biogeochemical Cycles*, *14*(1), 373–387. https://doi.org/10.1029/1999GB900091

Pfeil, B., Olsen, A., Baker, D., Hankin, S., Koyuk, H., Kozyr, A., et al. (2013). A uniform, quality controlled Surface Ocean CO_2 Atlas (SOCAT). *Earth System Science Data*, *5*(1), 125–143. https://doi.org/10.5194/essd-5-125-2013

Le Quéré, C., Andrew, R. M., Friedlingstein, P., Sitch, S., Pongratz, J., Manning, A. C., et al. (2018). Global Carbon Budget 2017. *Earth System Science Data Discussions*, *10*, 405–448. https://doi.org/https://doi.org/10.5194/essd-10-405-2018

Regnier, P., Friedlingstein, P., Ciais, P., Mackenzie, F. T., Gruber, N., Janssens, I. A., et al. (2013). Anthropogenic perturbation of the carbon fluxes from land to ocean. *Nature Geoscience*, *6*(8), 597–607. https://doi.org/10.1038/ngeo1830

Resplandy, L., Keeling, R. F., Rödenbeck, C., Stephens, B. B., Khatiwala, S., Rodgers, K. B., et al. (2018). Revision of global carbon fluxes based on a reassessment of oceanic and riverine carbon transport. *Nature Geoscience*, *11*(7), 504–509. https://doi.org/10.1038/s41561-018-0151-3

Reynolds, R. W., Smith, T. M., Liu, C., Chelton, D. B., Casey, K. S., & Schlax, M. G. (2007). Daily high-resolution-blended analyses for sea surface temperature. *Journal of Climate*, *20*(22), 5473–5496. https://doi.org/10.1175/2007JCLI1824.1

Rödenbeck, C., Baker, D., Gruber, N., Iida, Y., Jacobson, A. R., Jones, S., et al. (2015). Data-based estimates of the ocean carbon sink variability - First results of the Surface Ocean pCO_2 Mapping intercomparison (SOCOM). *Biogeosciences*, *12*(23), 7251–7278. https://doi.org/10.5194/bg-12-7251-2015

Roobaert, A., Laruelle, G. G., Landschützer, P., & Regnier, P. (2018). Uncertainty in the global oceanic CO_2 uptake induced by wind forcing: Quantification and spatial analysis. *Biogeosciences*, *15*(6), 1701–1720. https://doi.org/10.5194/bg-15-1701-2018

Sabine, C. L., Hankin, S., Koyuk, H., Baker, D., Pfeil, B., Olsen, A., et al. (2013). Surface Ocean CO_2 Atlas (SOCAT) gridded data products. *Earth System Science Data*, *5*(1), 145–153. https://doi.org/10.5194/essd-5-145-2013

Schuster, U., McKinley, G. A., Bates, N., Chevallier, F., Doney, S. C., Fay, a. R., et al. (2013). An assessment of the Atlantic and Arctic sea–air CO_2 fluxes, 1990–2009. *Biogeosciences*, *10*(1), 607–627. https://doi.org/10.5194/bg-10-607-2013

Shadwick, E. H., Thomas, H., Comeau, A., Craig, S. E., Hunt, C. W., & Salisbury, J. E. (2010). Air-sea CO_2 fluxes on the Scotian Shelf: Seasonal to multi-annual variability. *Biogeosciences*, *7*(11), 3851–3867. https://doi.org/10.5194/bg-7-3851-2010

Shadwick, E. H., Thomas, H., Azetsu-Scott, K., Greenan, B. J. W., Head, E., & Horne, E. (2011). Seasonal variability of dissolved inorganic carbon and surface water pCO_2 in the Scotian Shelf region of the Northwestern Atlantic. *Marine Chemistry*, *124*(1–4), 23–37. https://doi.org/10.1016/j.marchem.2010.11.004

Sweeney, C., Gloor, E., Jacobson, A. R., Key, R. M., McKinley, G. A., Sarmiento, J. L., & Wanninkhof, R. (2007). Constraining global air-sea gas exchange for CO_2 with recent bomb ^{14}C measurements. *Global Biogeochemical Cycles*, *21*(2), 1–10. https://doi.org/10.1029/2006GB002784

Takahashi, T., Sutherland, S. C., Wanninkhof, R., Sweeney, C., Feely, R. A., Chipman, D. W., et al. (2009). Climatological mean and decadal change in surface ocean pCO_2, and net sea-air CO_2 flux over the global oceans. *Deep Sea Research*

Part II: Topical Studies in Oceanography, *56*(8), 554–577. https://doi.org/10.1016/j.dsr2.2008.12.009.Figure

Takahashi, T., Sweeney, C., Hales, B., Chipman, D., Newberger, T., Goddard, J., et al. (2012). The Changing Carbon Cycle in the Southern Ocean. *Oceanography*, *25*(3), 26–37. https://doi.org/10.5670/oceanog.2012.71

Takahashi, T., Sutherland, S. C., & Kozyr, A. (2016). Global Ocean Surface Water Partial Pressure of CO_2 Database: Measurements Performed During 1957–2015 (Version 2015), ORNL/CDIAC-160, NDP-088(V2015). *Carbon Dioxide Information Analysis Center, Oak Ridge National Laboratory, US Department of Energy, Oak Ridge, Tennessee,*. https://doi.org/https://doi.org/10.3334/CDIAC/OTG.NDP088(V2015)

Tsunogai, S., Watanabe, S., & Sato, T. (1999). Is there a "continental shelf pump"for the absorption of atmospheric CO_2? *Tellus*, *51*, 701–712. https://doi.org/10.3402/tellusb.v51i3.16468

Turi, G., Lachkar, Z., & Gruber, N. (2014). Spatiotemporal variability and drivers of pCO_2 and air-sea CO_2 fluxes in the California Current System: An eddy-resolving modeling study. *Biogeosciences*, *11*(3), 671–690. https://doi.org/10.5194/bg-11-671-2014

Wanninkhof, R. (1992). Relationship Between Wind Speed and Gas Exchange. *Journal of Geophysical Research*, *97*(92), 7373–7382. https://doi.org/10.1029/92JC00188

Wanninkhof, R. (2014). Relationship between wind speed and gas exchange over the ocean revisited. *Limnology and Oceanography: Methods*, *12*, 351–362. https://doi.org/10.1029/92JC00188

Wanninkhof, R., & Trinanes, J. (2017). The impact of changing wind speeds on gas transfer and its effect on global air-sea CO_2 fluxes. *Global Biogeochemical Cycles*. https://doi.org/10.1002/2016GB005592

Wanninkhof, R., Asher, W. E., Ho, D. T., Sweeney, C., & McGillis, W. R. (2009). Advances in quantifying air-sea gas exchange and environmental forcing. *Annual Review of Marine Science*, *1*(1), 213–244. https://doi.org/10.1146/annurev.marine.010908.163742

Wanninkhof, R., Park, G.-H., Takahashi, T., Sweeney, C., Feely, R., Nojiri, Y., et al. (2013). Global ocean carbon uptake: Magnitude, variability and trends. *Biogeosciences*, *10*(3), 1983–2000. https://doi.org/10.5194/bg-10-1983-2013

Weiss, A., Kuss, J., Peters, G., & Schneider, B. (2007). Evaluating transfer velocity-wind speed relationship using a long-term series of direct eddy correlation CO_2 flux measurements. *Journal of Marine Systems*, *66*(1–4), 130–139. https://doi.org/10.1016/j.jmarsys.2006.04.011

Weiss, R. F. (1974). Carbon dioxide in water and seawater: the solubility of a non-ideal gas. *Marine Chemistry*, *2*, 203–215. https://doi.org/10.1017/CBO9781107415324.004

Winterfeldt, J., & Weisse, R. (2008). Surface marine wind from the NCEP/NCAR and NCEP/DOE-II reanalyses. *18th Symposium on Boundary Layers*.

Yasunaka, S., Murata, A., Watanabe, E., Chierici, M., Fransson, A., van Heuven, S., et al. (2016). Mapping of the air-sea CO_2 flux in the Arctic Ocean and its adjacent seas: Basin-wide distribution and seasonal to interannual variability. *Polar Science*, *10*(3), 323–334. https://doi.org/10.1016/j.polar.2016.03.006

	Coastal seas	Open ocean	Global ocean
FCO_2 (Tg C yr^{-1})			
Indian	10 (±5)	-331 (±190)	-322 (±190)
Atlantic	-27 (±3)	-366 (±29)	-393 (±29)
Pacific	-54 (±9)	-331 (±89)	-386 (±90)
Southern Ocean*	-17 (±3)	-258 (±123)	-275 (±123)
> 60° N	-88** (±7)	-87 (±21)	-175 (±22)
Marginal seas	-18 (±2)	-	-18 (±2)
Total	-195 (±18)	-1375 (±255)	-1570 (±256)
FCO_2 (Pg C yr^{-1})			
	-0.20 (±0.02)	-1.38 (±0.26)	-1.57 (±0.26)
Arctic basin***			-0.12 (±0.06)
Total with Arctic basin			-1.69 (±0.26)

*South of 45° S. **This value exclude marginal seas. With marginal seas included, a value of -98 Tg C yr^{-1} is obtained for all coastal regions located > 60° N. ***Schuster et al. (2013).

Table 1. Global integrated FCO_2, generated from a 18-year climatology (1998-2015), for the different oceanic basins (Tg C yr^{-1}). The partitioning of these basin-wide fluxes between coastal seas and the open ocean is also reported. Numbers in parentheses correspond to the FCO_2 uncertainties calculated according to section 2.5. Marginal seas include the Hudson Bay, the Baltic Sea, the Mediterranean Sea, the Red Sea, the Persian Gulf, and the Black Sea. By combining the coastal/open ocean estimates, the total integrated FCO_2 for the different oceanic basins as well as for the entire global ocean is evaluated (global ocean column).

N°	System name	Class	Surface area (10^3 km^2)			FCO_2 (mol C m^{-2} yr^{-1})						Integrated FCO_2 (Tg C yr^{-1})				
			BG 2016	LA 2014	This study	BG2016		LA2014		This study		BG2016		LA 2014	This study	
						mean	σ	mean	σ	mean	σ	mean	σ		mean	σ
1	North East Pacific	Subpolar	397	350	394	-2.29	0.17	-1.61	0.25	-1.59	0.6	-10.94	0.82	-6.78	-7.53	2.67
2	Californian current	EBC	118	208	186	-0.34	0.10	-0.05	0.50	-0.60	0.2	-0.48	0.15	-0.14	-1.33	0.48
3	Tropical East Pacific	Tropical	152	183	162	-0.12	0.05	0.09	0.60	0.00	0.1	-0.22	0.10	0.19	0.00	0.18
4	Peruvian upwelling current	EBC	138	143	121	1.44	0.80	0.65	0.60	-0.83*	0.6	2.39	1.33	1.07	-1.20	0.88
5	Southern America	Subpolar	1126	1190	1163	-1.51	0.13	-1.31	0.50	-1.24	0.5	-20.46	1.71	-18.72	-17.38	6.53
6	Brazilian current	WBC	475	484	497	-0.33	0.08	0.10	0.25	-0.12	0.3	-1.87	0.48	0.57	-0.72	1.55
7	Tropical West Atlantic	Tropical	479	488	490	0.86	0.10	0.07	0.60	0.25	0.3	4.93	0.55	0.39	1.49	1.86
8	Caribbean Sea	Tropical	303	358	289	0.10	0.10	0.81	0.60	0.80	0.2	0.37	0.35	3.46	2.77	0.53
9	Gulf of Mexico	Marginal sea	469	532	501	-0.79	0.11	-0.33	0.50	0.24	0.3	-4.48	0.63	-2.10	1.42	1.90
10	Florida upwelling	WBC	545	591	804	-2.25	0.21	-0.38	0.25	-0.83	0.2	-14.69	1.35	-2.72	-8.00	2.04
11	Sea of Labrador	Subpolar	576	638	342	-1.27	0.18	-1.72	0.60	-1.88	0.6	-8.81	1.24	-13.17	-7.70	2.38
12	Hudson Bay	Marginal sea	998	1064	1013	0.31	0.29	-	-	-1.38	0.1***	3.76	3.42	-	-16.81	1.04
13	Canadian Archipelago	Polar	1001	1145	1020	-0.52	0.06	-1.02	0.60	-0.40	0.1	-6.23	0.75	-13.99	-4.91	1.65
14	North Greenland	Polar	544	602	572	-0.97	0.15	-0.61	0.50	-0.93	0.2	-6.33	1.00	-4.40	-6.38	0.63
15	South Greenland	Polar	238	262	248	-3.35	0.44	-3.81	0.50	-2.90	0.3	-9.56	1.26	-11.97	-8.61	0.99
16	Norwegian Basin	Polar	141	162	142	-2.87	0.23	-1.72	0.25	-2.55	0.5	-4.86	0.40	-3.34	-4.34	0.83
17	North East Atlantic	Subpolar	1020	1073	1040	-2.16	0.12	-1.33	0.25	-1.10	0.2	-26.50	1.42	-17.17	-13.68	2.77

18	Baltic Sea	Marginal sea	324	364	336	0.30	0.07	0.51	0.50	-0.39	0.4	1.18	0.29	2.25	-1.58	1.66
19	Iberian upwelling	EBC	251	267	251	-1.13	0.12	0.04	0.25	-0.87	0.3	-3.39	0.35	0.12	-2.64	0.91
20	Mediterranean Sea	Marginal sea	423	529	474	-0.24	0.06	0.62	0.60	-0.01	0.1	-1.20	0.33	3.93	-0.07	0.51
21	Black Sea	Marginal sea	131	172	104	-0.24	0.11	-	-	-2.85	0.6	-0.38	0.17	-	-3.55	0.75
22	Moroccan upwelling	EBC	177	206	179	0.18	0.12	2.92	0.50	0.24**	0.6	0.39	0.26	7.22	0.52	1.20
23	Tropical East Atlantic	Tropical	225	259	259	0.09	0.08	-0.06	0.60	0.03	0.1	0.24	0.21	-0.17	0.09	0.29
24	South West Africa	EBC	300	298	295	0.43	0.40	-1.43	0.50	-1.06	0.8	1.54	1.45	-5.10	-3.76	2.66
25	Agulhas current	WBC	189	239	228	-1.20	0.09	-0.58	0.60	-0.39	0.4	-2.73	0.21	-1.66	-1.07	1.07
26	Tropical West Indian	Tropical	46	68	60	-0.06	0.08	1.00	0.60	0.30	0.2	-0.03	0.04	0.82	0.22	0.12
27	West Arabian Sea	Indian margins	82	92	81	0.35	0.04	1.14	0.60	-0.11**	0.4	0.34	0.04	1.26	-0.11	0.42
28	Red Sea	Marginal sea	158	174	165	0.24	0.03	0.16	0.60	0.67	0.1	0.46	0.07	0.33	1.33	0.20
29	Persian Gulf	Marginal sea	208	233	217	0.04	0.08	-	-	0.85	0.1***	0.09	0.20	-	2.20	0.26
30	East Arabian Sea	Indian margins	298	317	317	0.21	0.12	0.67	0.60	0.61	0.1***	0.75	0.43	2.56	2.31	0.34
31	Bay of Bengal	Indian margins	197	203	204	-0.69	0.12	-0.22	0.60	0.15	0.03***	-1.64	0.28	-0.53	0.36	0.08
32	Tropical East Indian	Indian margins	727	763	755	-0.06	0.07	-0.02	0.60	0.16	0.1	-0.48	0.57	-0.17	1.46	0.74
33	Leeuwin current	EBC	81	117	112	-2.05	0.15	-0.98	0.25	-0.49	0.2	-2.01	0.15	-1.38	-0.66	0.25
34	South Australia	Subpolar	392	436	429	-1.37	0.18	-1.14	0.50	-0.28	0.3	-6.44	0.86	-5.98	-1.44	1.60
35	East Australian current	WBC	98	130	133	-1.74	0.18	-1.09	0.25	-0.74	0.2	-2.04	0.21	-1.70	-1.18	0.35
36	New Zealand	Subpolar	263	286	266	-1.23	0.16	-1.25	0.50	-0.90	0.2	-3.88	0.50	-4.27	-2.88	0.49
37	North Australia	Tropical	2278	2292	2369	-0.29	0.11	0.44	0.60	0.31	0.1	-7.87	3.11	12.12	8.72	2.68

38	South East Asia	Tropical	2130	2160	2196	-0.29	0.07	-0.91	0.60	0.07	0.2	-7.34	1.91	-23.61	1.77	4.22
39	China Sea and Kuroshio	WBC	1132	1129	1172	-1.99	0.15	-1.41	0.60	-0.59	0.1	-27.05	1.99	-19.10	-8.30	2.03
40	Sea of Japan	Marginal sea	233	147	249	-3.07	0.17	-3.47	0.50	-1.44	0.6	-8.61	0.48	-6.11	-4.32	1.84
41	Sea of Okhotsk	Marginal sea	933	952	953	-1.66	0.07	1.31	0.60	-1.85	0.6	-18.62	0.76	1.50	-21.18	7.10
42	North West Pacific	Subpolar	1025	1000	1058	-1.85	0.14	-0.70	0.60	-1.46	0.5	-22.76	1.73	-8.42	-18.58	6.17
43	Siberian Shelves	Polar	1848	1889	1864	-0.47	0.10	-0.90	0.60	-0.50	0.1	-10.50	2.12	-20.32	-11.12	1.82
44	Barents and Kara seas	Polar	1559	1680	1609	-0.75	0.14	-1.60	0.60	-1.78	0.4	-14.18	2.59	-32.23	-34.41	7.75
45	Antarctic Shelves	Polar	2452	2936	2693	-0.90	0.14	-0.15	0.50	-0.12	0.1	-26.63	3.99	-5.38	-3.80	2.55

* Due to the scarcity of the data in SOCATv4 dataset for this region, the pCO_2 product of Laruelle et al. (2017) underestimates the observed pCO_2 and does not reproduce the high FCO_2 source (5.7 mol C m^{-2} yr^{-1}) of the region observed by Friederich et al. (2008).

** A pCO_2 underestimation is also observed for these two regions because of the scarcity in data to train the algorithm for MARCATS 22 (Laruelle et al., 2017) and given that the monsoon-driven summer upwelling in coastal seas is not captured by the SOM-FFN in MARCATS 27.

*** The scarcity in data in MARCATS 12, 29, 30 and 31 does not allow one to calculate σ_{pCO2} for these regions in the total FCO_2 uncertainty calculation.

Table S1. Surface area (10^3 km^2), air-sea CO_2 exchange rate (FCO_2, mol C m^{-2} yr^{-1}) and integrated FCO_2 (Tg C yr^{-1}) calculated for each MARCATS regions. BG2016 and LA2014 refer to the study of Bourgeois et al. (2016) and of Laruelle et al. (2014), respectively. σ in the LA2014 study corresponds to the uncertainties associated to the data coverage in time and space when they derived FCO_2. For BG2016, uncertainty corresponds to the FCO_2 interannual variability for the 1993-2012 period. In this study, FCO_2 uncertainties are calculated according to section 2.5.

Figure 1. Discretization of the coastal seas into 45 MARCATS (Margins and CATchment Segmentation, Laruelle et al., 2013)**.** These MARCATS are also grouped into seven major classes following Liu et al. (2010): Eastern and Western (MARCATS 6, 10, 25, 35, 39) boundary currents (EBC and WBC respectively), polar (MARCATS 13, 14, 15, 16, 43, 44, 45) and subpolar (MARCATS 1, 5, 11, 17, 34, 36, 42) margins, tropical margins (MARCATS 3, 7, 8, 23, 26, 37, 38), Indian margins (MARCATS 27, 30, 31, 32) and marginal seas (MARCATS 9, 12, 18, 20, 21, 28, 29, 40, 41).

Figure 2. Global distributions of the annually averaged mean air-sea CO_2 exchange rate (FCO_2, mol C m^{-2} yr^{-1}) generated from a 18-year climatology (1998-2015) (a) for the coastal seas and (b) for the open ocean. A positive FCO_2 value represents a source of CO_2 for the atmosphere, and vice versa for negative FCO_2.

Figure 3. (a) Air-sea CO_2 exchange rate (FCO_2, mol C m^{-2} yr^{-1}) aggregated per MARCATS region as a function of latitude. Colors correspond to the seven major classes (see Figure 1, Liu et al., 2010). MARCATS discussed in section 3.1 are reported with their respective number. (b) Mean integrated FCO_2 (Tg C yr^{-1}) in the different MARCATS classes. For both panels, error bars correspond to the FCO_2 uncertainties calculated as described in section 2.5.

Figure 4. (a) Amplitude of the spatial variability within latitudinal bands of the mean air-sea gas exchange rate of CO_2 (FCO_2, mol C m^{-2} yr^{-1}) for the coastal seas (in red) and the open ocean (in blue). Shaded areas correspond to the FCO_2 longitudinal variability. (b-c) Spatial variation by 1 degree latitudinal bands of the integrated FCO_2 (Tg C yr^{-1}) and the surface area (10^6 km^2) for the open ocean and for the coastal seas, respectively.

Figure 5. Spatial distribution of the amplitude of the seasonal FCO_2 variability (mol C m^{-2} yr^{-1}) (a) calculated as the root-mean-square for each grid cell of the monthly FCO_2 anomalies ($\mathrm{RMS}_{FCO_2'}$). (b-f) Seasonal FCO_2 anomaly (FCO_2' in mol C m^{-2} yr^{-1}, black lines) in different latitudinal bands calculated as the mean of the surface weighted average FCO_2' of all grid cells pertaining to that band. Dotted lines correspond to uncertainties calculated according to section 2.5. For each panel, a positive value for a given month implies that the FCO_2 is a stronger source/weaker sink of CO_2 than the 18-year mean FCO_2 calculated for this latitudinal band. A negative value means a stronger sink/weaker source. Winter covers the months of January, February and March in the Northern Hemisphere and of July, August and September in the Southern Hemisphere. The seasonal FCO_2' profile is plotted twice for each latitudinal band in order to better visualize the temporal pattern. The root-mean-square of the monthly FCO_2 anomalies is also calculated for each latitudinal bands ($\mathrm{RMS}_{FCO_2'}$, mol C m^{-2} yr^{-1}) and differs from the $\mathrm{RMS}_{FCO_2'}$ in panel (a), which is calculated at the grid cell level.

Figure 6. Spatial distribution of the amplitude of the seasonal FCO_2 variability (mol C m^{-2} yr^{-1}) calculated for each MARCATS region as a function of their latitude. Colors represent the MARCATS classes (see Figure 1). For each MARCATS, the root-mean-square of the monthly FCO_2 anomalies is

calculated ($RMS_{FCO_2'}$, mol C m^{-2} yr^{-1}) and differs from the $RMS_{FCO_2'}$ calculated at the grid cell level. MARCATS discussed in section 3.3 are reported with their respective MARCATS number. The RMS value of 3.4 mol C m^{-2} yr^{-1} for the Baltic Sea (MARCATS 18, latitude of 64° N) is not shown in the figure.

Figure 7. Contributions of the different drivers (β_x with x = (a) ΔpCO_2, (b) the wind speed, (c) the sea-ice cover and (d) the cross-correlation between the 3 terms) to the seasonal FCO_2' in mol C m^{-2} yr^{-1}. For each map, β is calculated on each grid cell using equation 8. A value close to one indicates that a term contributes strongly to FCO_2' whereas a value of 0 shows that FCO_2' is insensitive to that term. Negative values indicate that a term is anti-correlated with FCO_2'. β are then multiplied by the root-mean-square (RMS) of the total FCO_2' to highlight regions with high absolute seasonal variability and are thus expressed in mol C m^{-2} yr^{-1}.

Figure 8. Seasonal FCO_2 anomaly (FCO_2' in mol C m^{-2} yr^{-1}, black lines) in different latitudinal bands calculated as the mean of the surface weighted average FCO_2' of all grid cells pertaining to that band. For each panel, a positive value for a given month implies that the FCO_2 is a stronger source/weaker sink of CO_2 compared to the 18-year mean FCO_2 calculated for this latitudinal band. A negative value means a stronger sink/weaker source. The root-mean-square of the monthly FCO_2 anomalies is also calculated for each latitudinal band ($RMS_{FCO_2'}$, mol C m^{-2} yr^{-1}). The FCO_2 seasonal variability associated to the sea-ice cover, ΔpCO_2, wind speed and the cross-correlation between the 3 terms is represented in blue, red, green and pink, respectively. Winter covers the months of January, February and March in the Northern Hemisphere and of July, August and September in the Southern Hemisphere.

Figure 1.

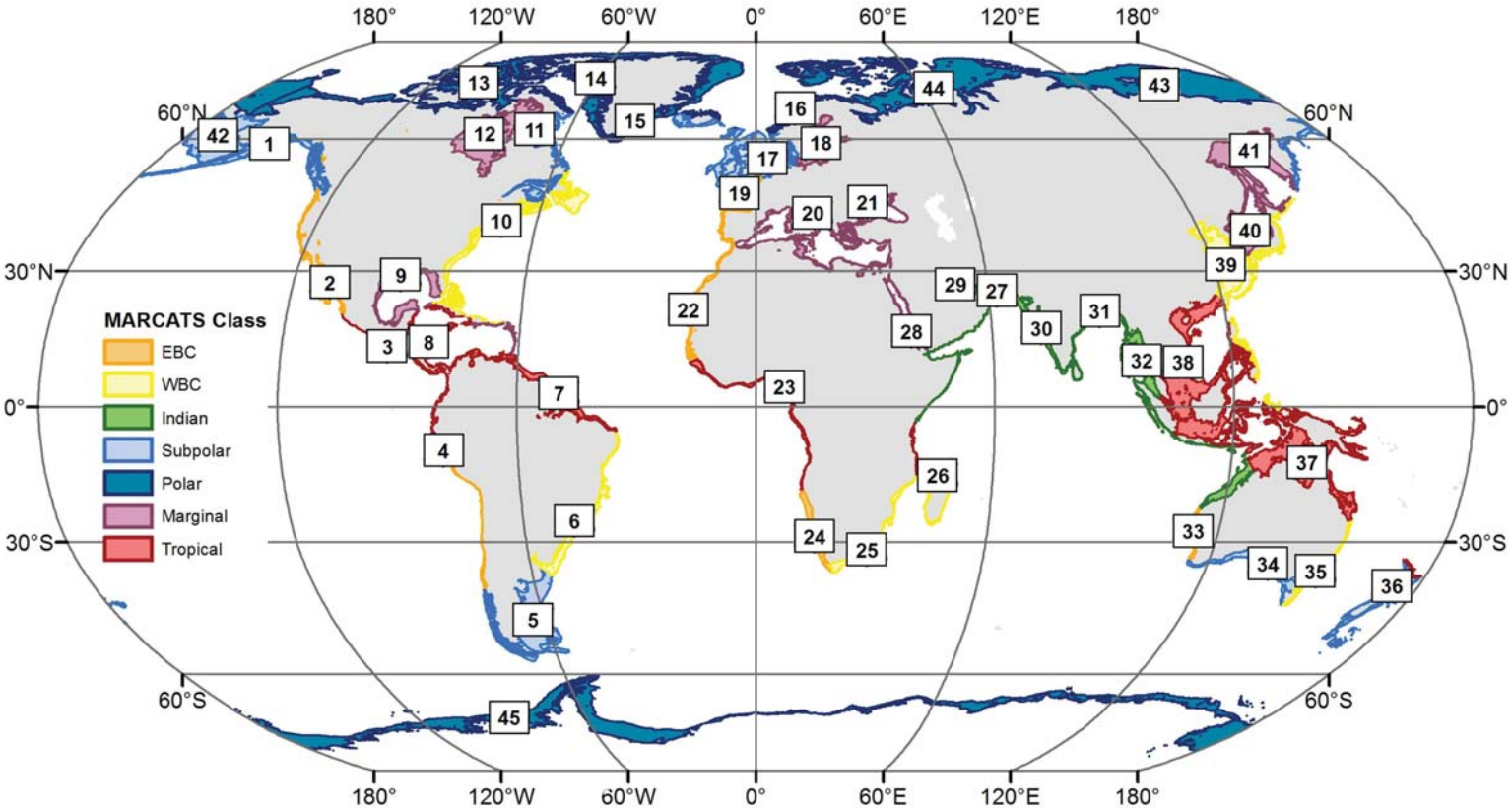
180°
120°W
60°W
0°
60°E
120°E
180°
60°N
30°N
0°
30°S
60°S
MARCATS Class
EBC
WBC
Indian
Subpolar
Polar
Marginal
Tropical
1
2
3
4
5
6
7
8
9
10
11
12
13
14
15
16
17
18
19
20
21
22
23
24
25
26
27
28
29
30
31
32
33
34
35
36
37
38
39
40
41
42
43
44
45

Figure 2.

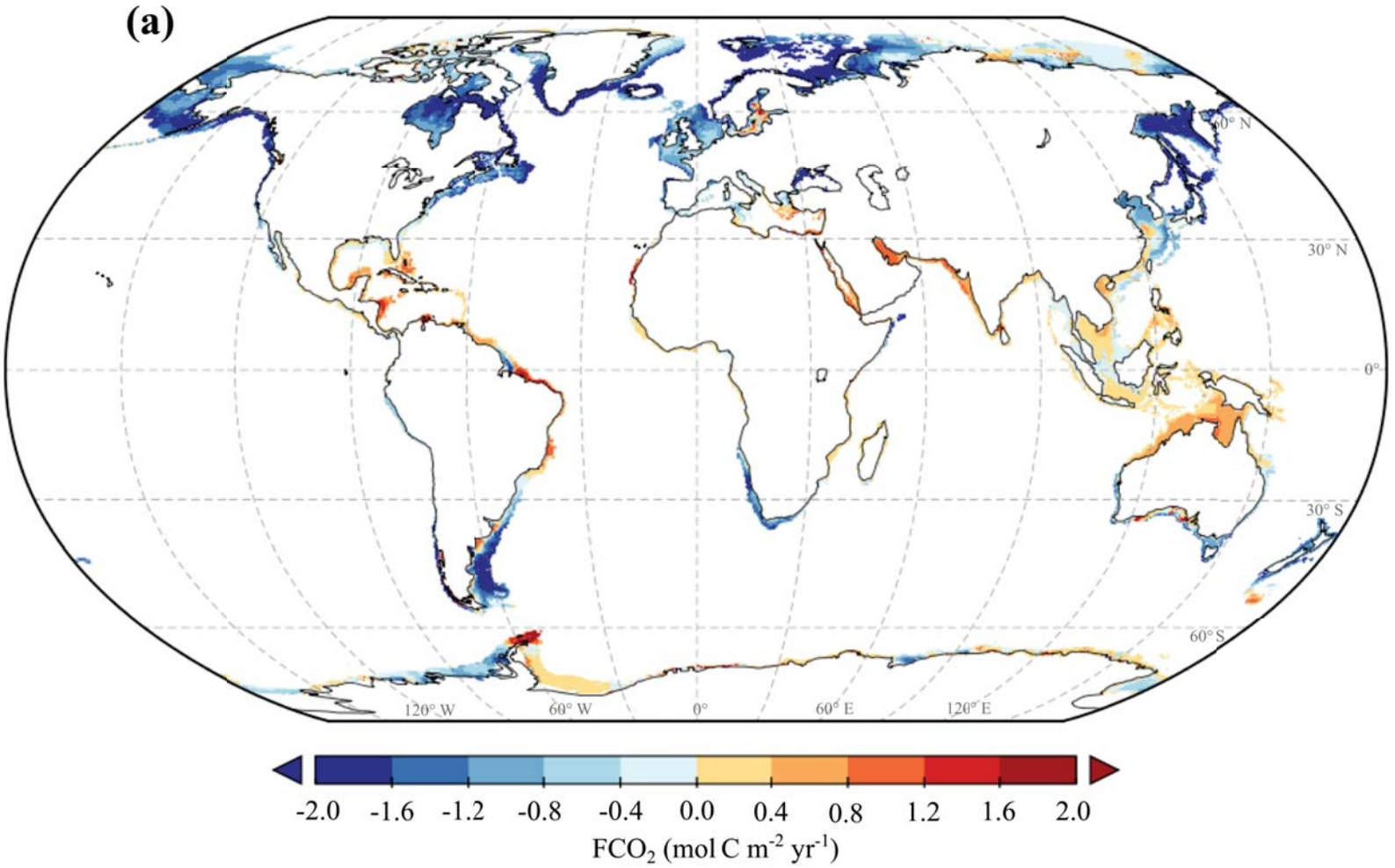
(a)
60° N
30° N
0°
30° S
60° S
120° W
60° W
0°
60° E
120° E
-2.0 -1.6 -1.2 -0.8 -0.4 0.0 0.4 0.8 1.2 1.6 2.0
FCO2 (mol C m-2 yr-1)

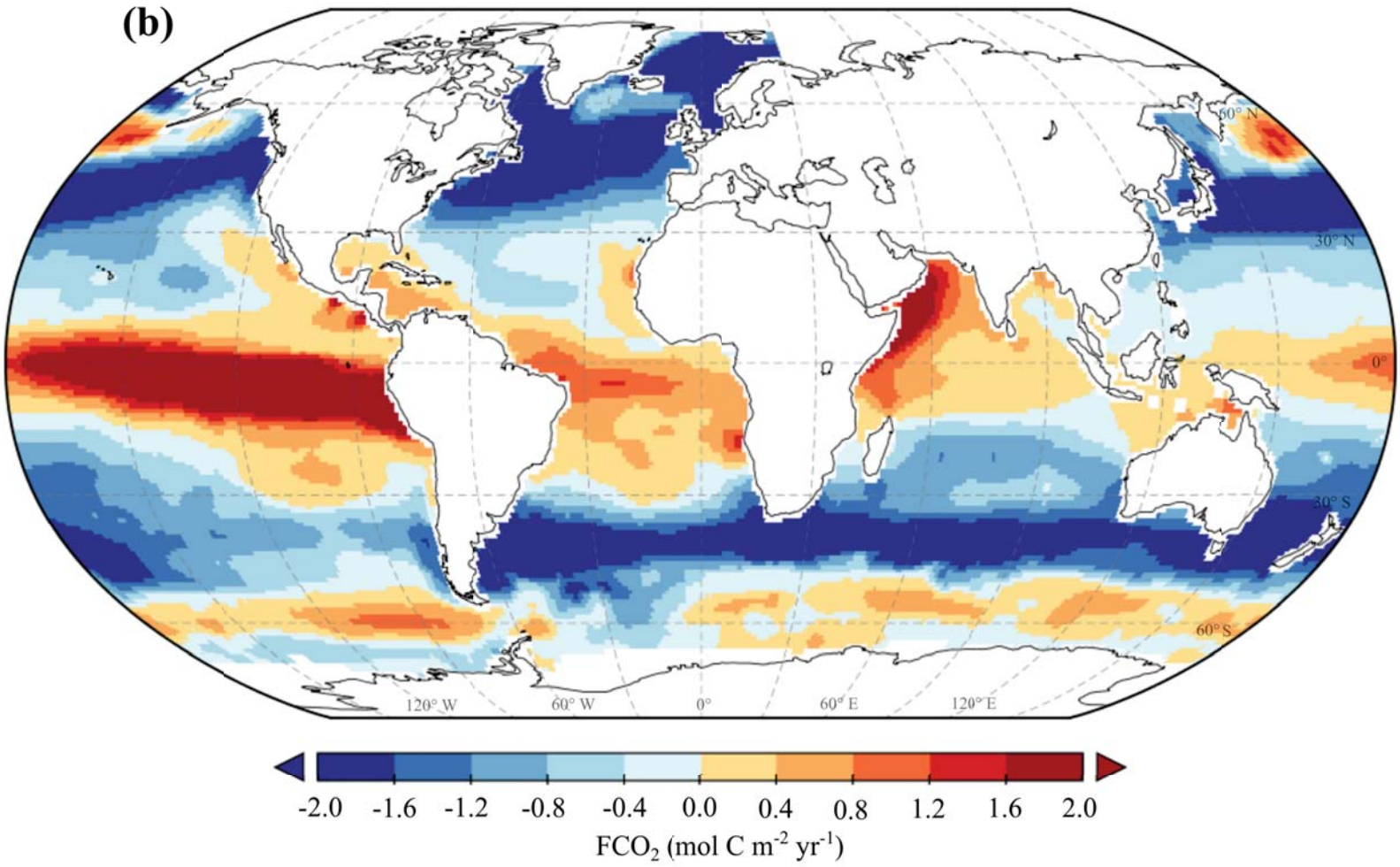
(b)
60° N
30° N
0°
30° S
60° S
120° W
60° W
0°
60° E
120° E
-2.0 -1.6 -1.2 -0.8 -0.4 0.0 0.4 0.8 1.2 1.6 2.0
FCO2 (mol C m-2 yr-1)

Figure 3.

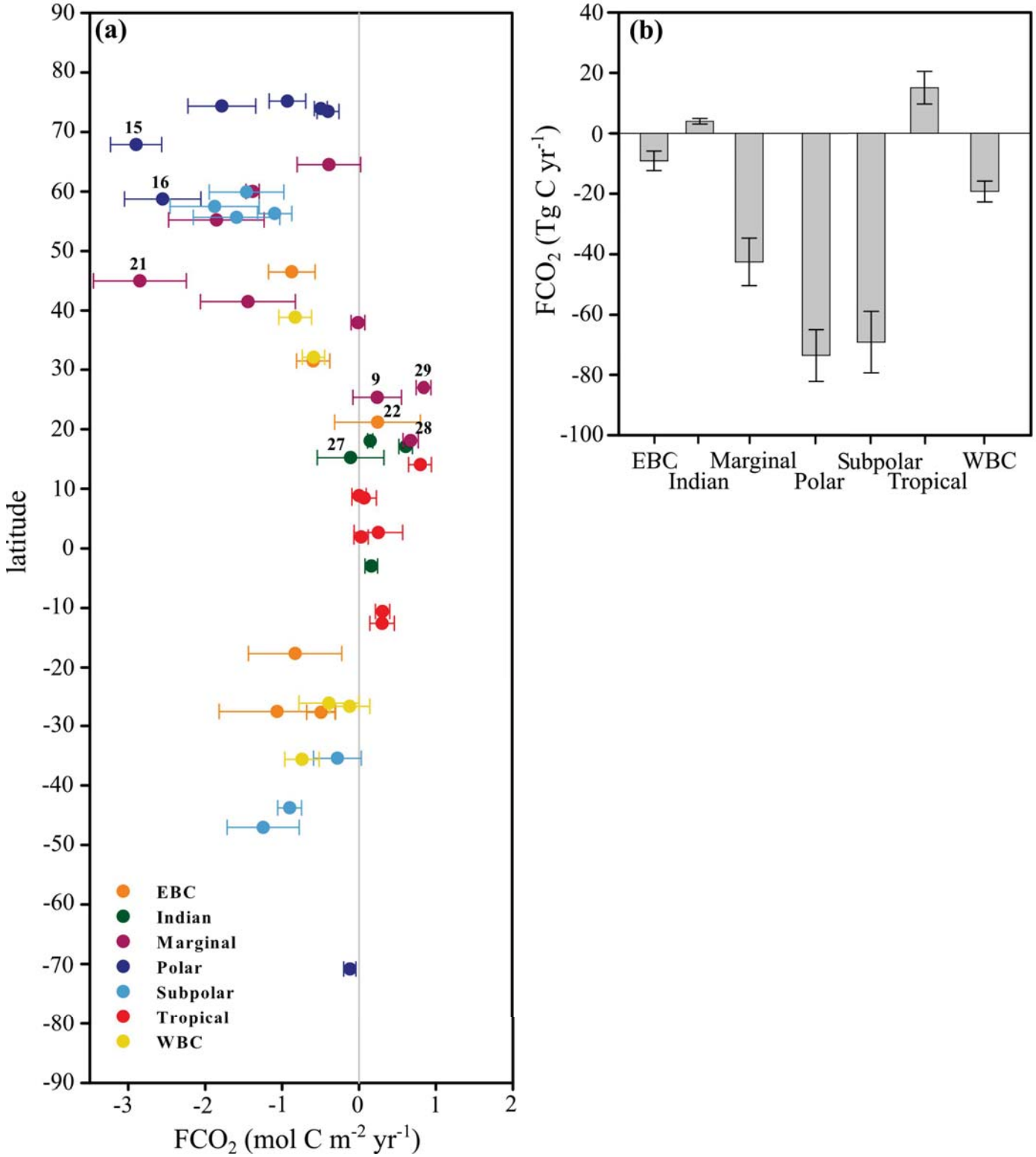
(a)
latitude
FCO2 (mol C m-2 yr-1)
15
16
21
9
29
22
28
27
EBC
Indian
Marginal
Polar
Subpolar
Tropical
WBC
(b)
FCO2 (Tg C yr-1)
EBC
Indian
Marginal
Polar
Subpolar
Tropical
WBC

Figure 4.

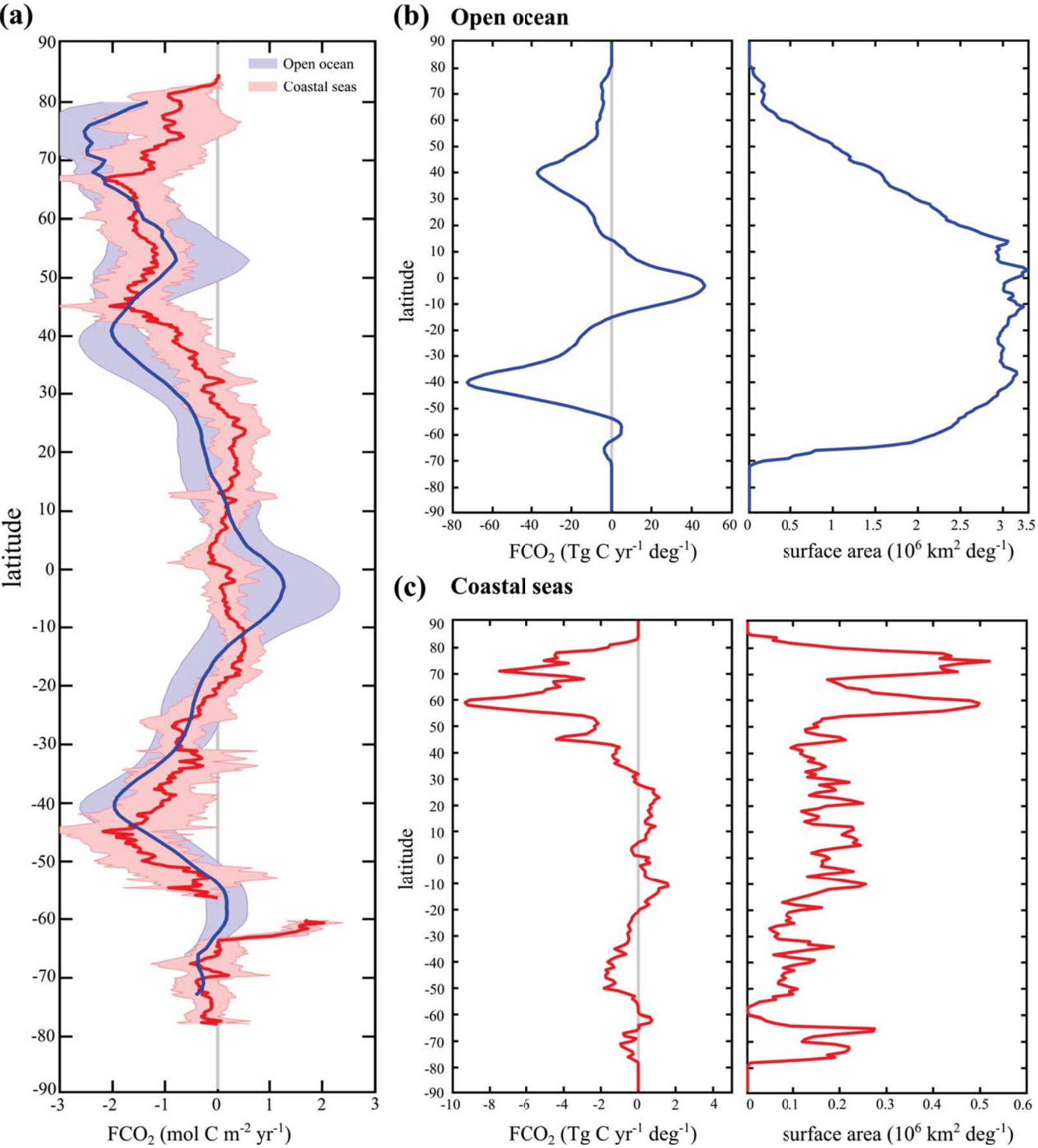
(a)
Open ocean
Coastal seas
latitude
FCO2 (mol C m-2 yr-1)
(b) Open ocean
latitude
FCO2 (Tg C yr-1 deg-1)
surface area (10^6 km^2 deg-1)
(c) Coastal seas
latitude
FCO2 (Tg C yr-1 deg-1)
surface area (10^6 km^2 deg-1)

Figure 5.

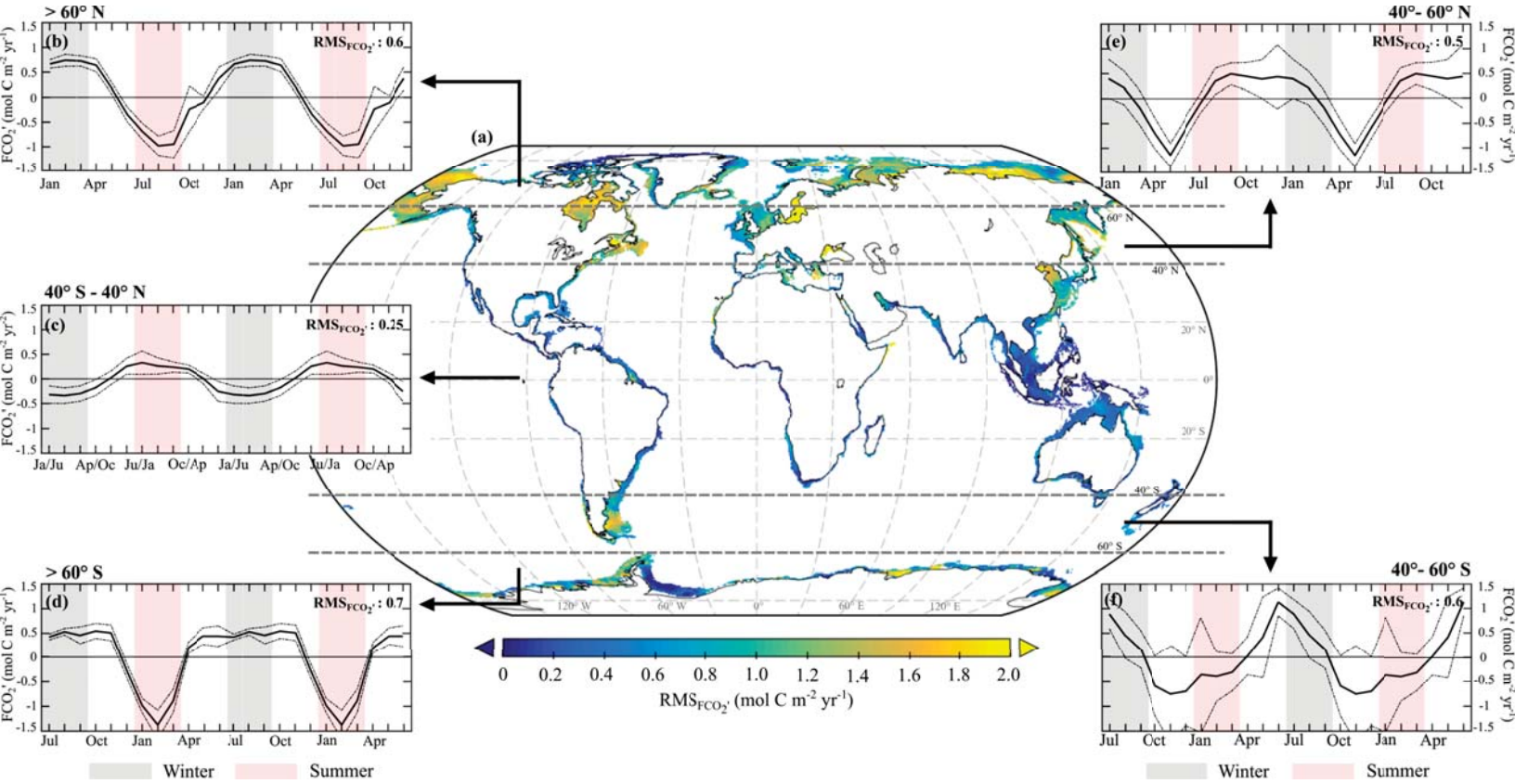
> 60° N
(b)
RMS$_{FCO_2'}$: 0.6
40° S - 40° N
(c)
RMS$_{FCO_2'}$: 0.25
> 60° S
(d)
RMS$_{FCO_2'}$: 0.7
40°- 60° N
(e)
RMS$_{FCO_2'}$: 0.5
40°- 60° S
(f)
RMS$_{FCO_2'}$: 0.6
(a)
FCO$_2$' (mol C m^{-2} yr^{-1})
Jan Apr Jul Oct Jan Apr Jul Oct
Ja/Ju Ap/Oc Ju/Ja Oc/Ap Ja/Ju Ap/Oc Ju/Ja Oc/Ap
Jul Oct Jan Apr Jul Oct Jan Apr
Winter
Summer
60° N
40° N
20° N
0°
20° S
40° S
60° S
120° W
60° W
0°
60° E
120° E
0 0.2 0.4 0.6 0.8 1.0 1.2 1.4 1.6 1.8 2.0
RMS$_{FCO_2'}$ (mol C m^{-2} yr^{-1})

Figure 6.

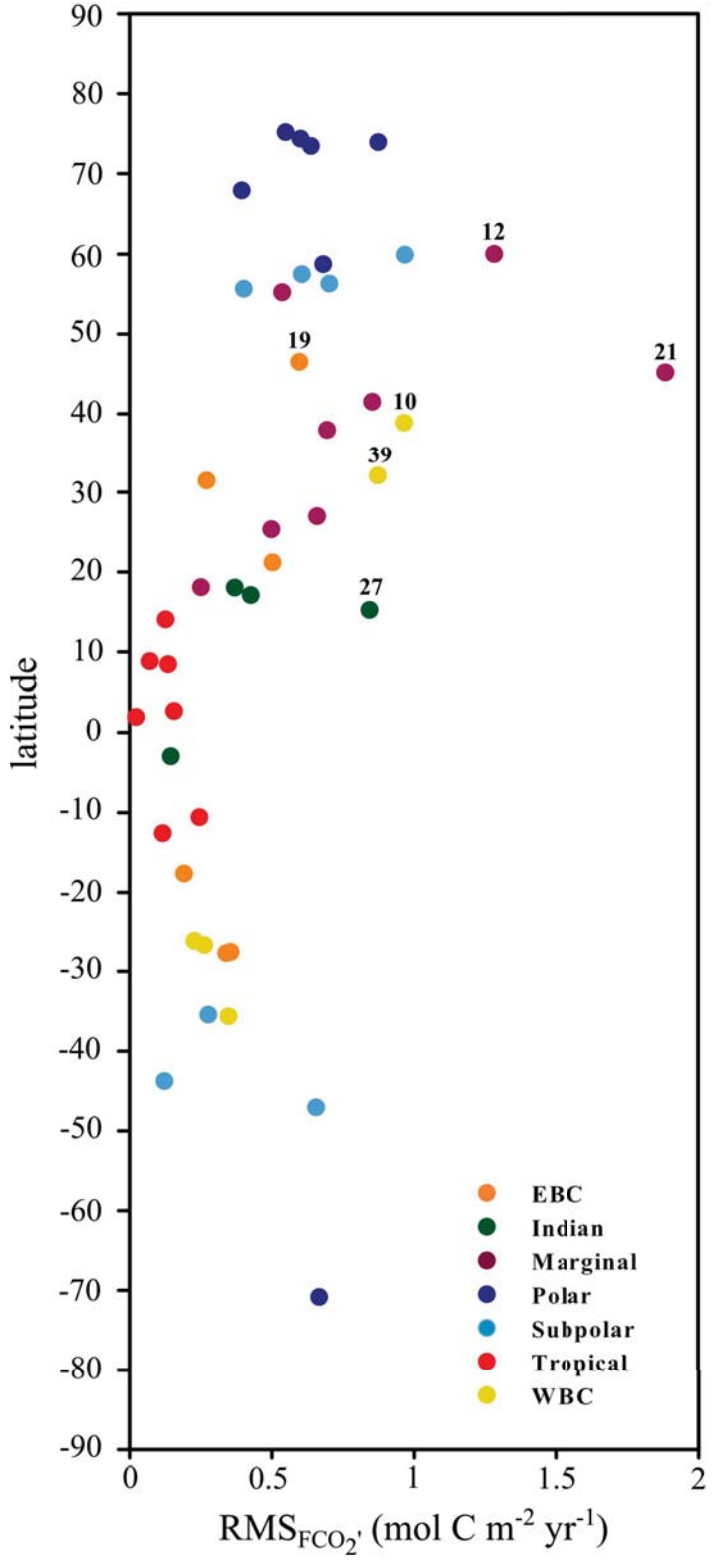
90
80
70
60
50
40
30
20
10
0
-10
-20
-30
-40
-50
-60
-70
-80
-90
latitude
0
0.5
1
1.5
2
RMS$_{FCO_2'}$ (mol C m^{-2} yr^{-1})
12
21
19
10
39
27
EBC
Indian
Marginal
Polar
Subpolar
Tropical
WBC

Figure 7.

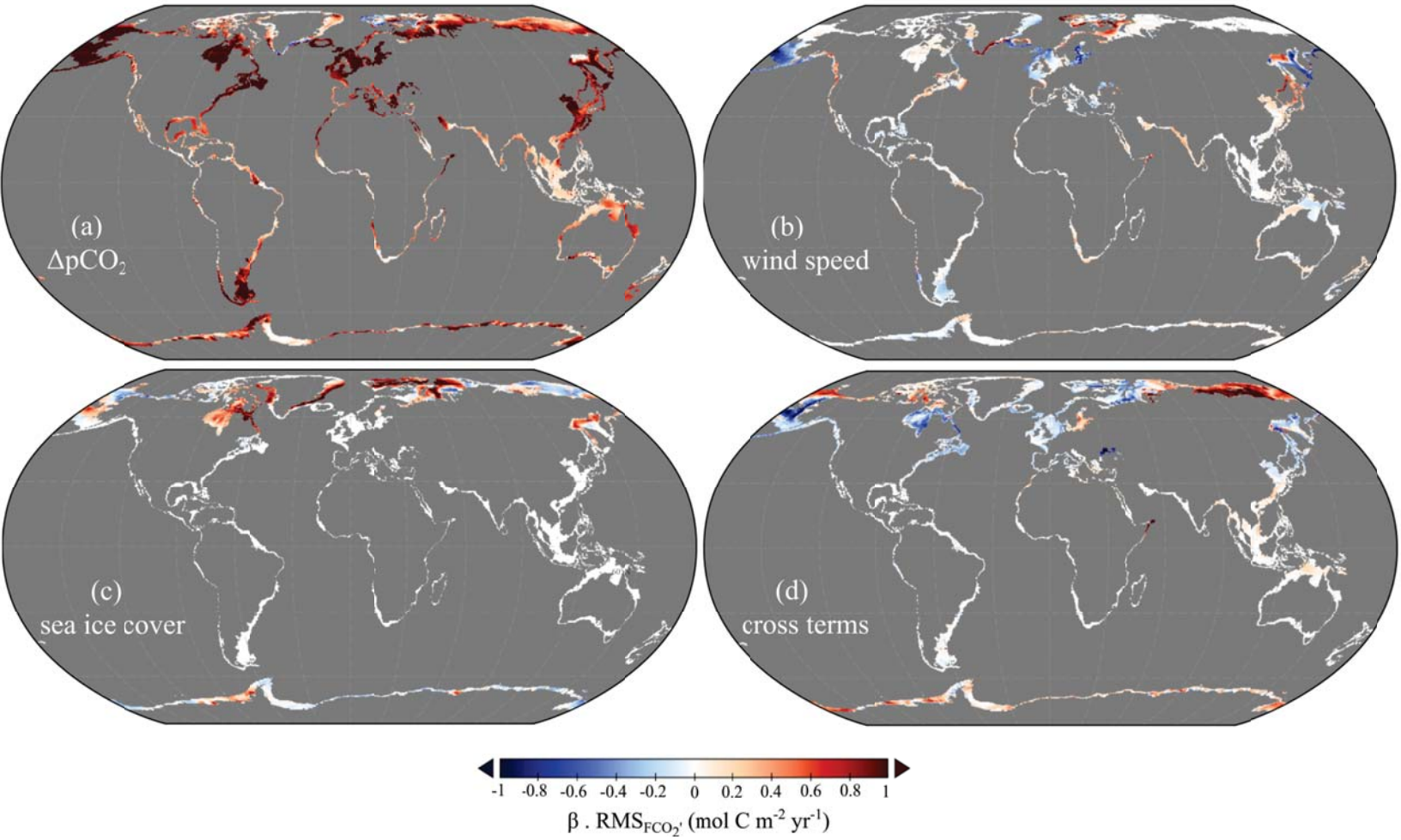
(a)
ΔpCO2
(b)
wind speed
(c)
sea ice cover
(d)
cross terms
-1 -0.8 -0.6 -0.4 -0.2 0 0.2 0.4 0.6 0.8 1
β . RMSFCO2' (mol C m-2 yr-1)

Figure 8.

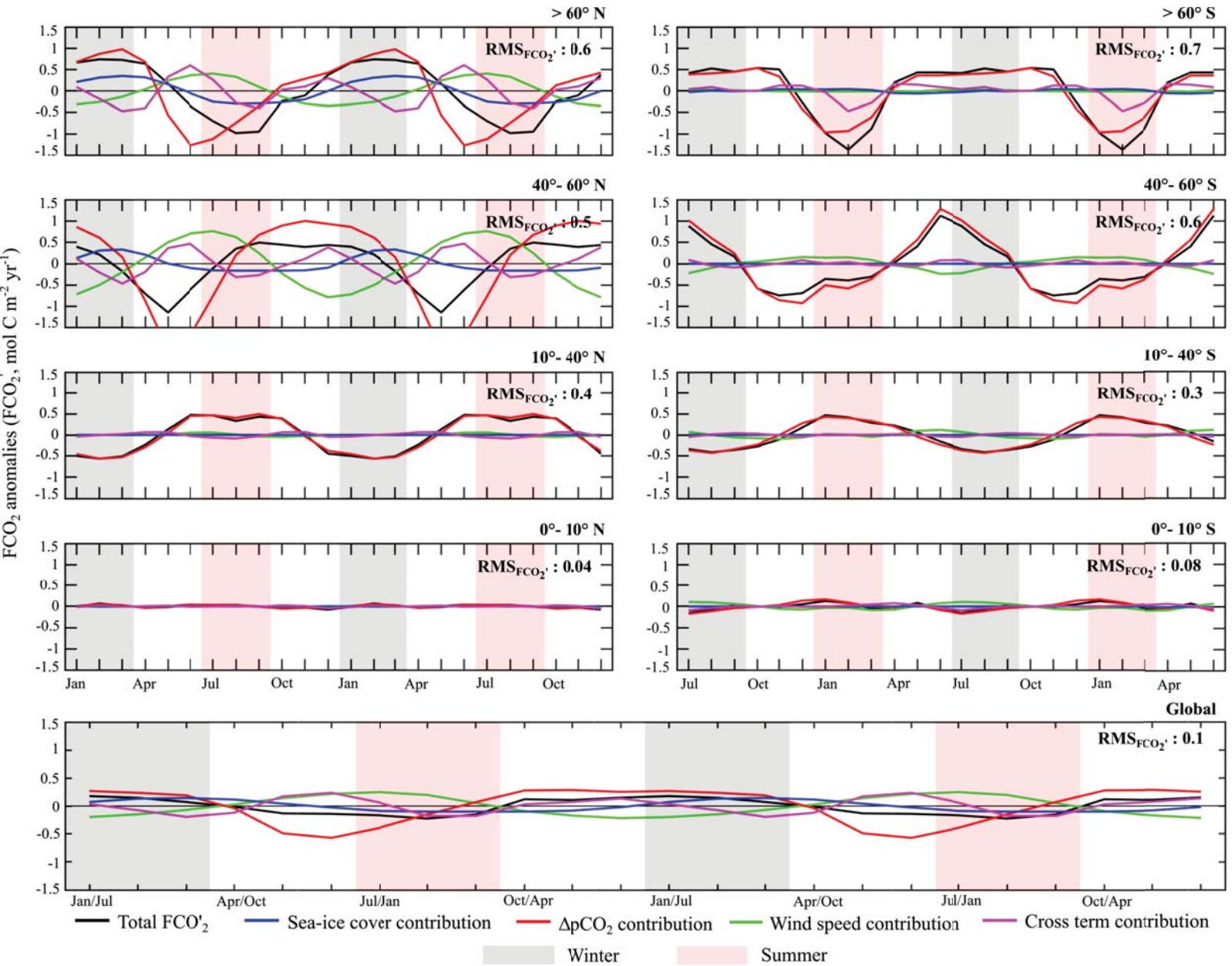
> 60° N
RMS$_{FCO_2'}$: 0.6
> 60° S
RMS$_{FCO_2'}$: 0.7
40°- 60° N
RMS$_{FCO_2'}$: 0.5
40°- 60° S
RMS$_{FCO_2'}$: 0.6
10°- 40° N
RMS$_{FCO_2'}$: 0.4
10°- 40° S
RMS$_{FCO_2'}$: 0.3
0°- 10° N
RMS$_{FCO_2'}$: 0.04
0°- 10° S
RMS$_{FCO_2'}$: 0.08
Global
RMS$_{FCO_2'}$: 0.1
FCO$_2$ anomalies (FCO$_2'$, mol C m^{-2} yr^{-1})
Jan
Apr
Jul
Oct
Jan/Jul
Apr/Oct
Jul/Jan
Oct/Apr
Total FCO'$_2$
Sea-ice cover contribution
ΔpCO$_2$ contribution
Wind speed contribution
Cross term contribution
Winter
Summer